

# Ion Mobility in Crystalline Battery Materials

Mohsen Sotoudeh, Sebastian Baumgart, Manuel Dillenz, Johannes Döhn, Katrin Forster-Tonigold, Katharina Helmbrecht, Daniel Stottmeister, and Axel Groß\*

**Ion mobility in electrolytes and electrodes is an important performance parameter in electrochemical devices, particularly in batteries. In this review, the authors concentrate on the charge carrier mobility in crystalline battery materials where the diffusion basically corresponds to hopping processes between lattice sites. However, in spite of the seeming simplicity of the migration process in crystalline materials, the factors governing mobility in these materials are still debated. There are well-accepted factors contributing to the ion mobility such as the size and the charge of the ions, but they are not sufficient to yield a complete picture of ion mobility. In this review, possible factors influencing ion mobility in crystalline battery materials are critically discussed. To gain insights into these factors, chemical trends in batteries, both as far as the charge carriers as well as the host materials are concerned, are discussed. Furthermore, fundamental questions, for example, about the nature of the migrating charge carriers, are also addressed.**

ion mobility. In recent years, significant progress has been made in our conceptual understanding of ion mobility in crystalline electrode materials, especially concerning the role of non-ionic interaction between the migrating ion and the host lattice.<sup>[2–5]</sup> In this review, we will discuss the materials' properties that correlate with ionic conductivity, in particular with the height of the activation barrier, using the descriptor concept. Both experimental and theoretical studies will be addressed in order to establish strategies to identify solid electrolytes and electrodes with improved mobility.

This review is concerned with the ion mobility in crystalline battery materials, including both electrolytes and electrodes. There is a fundamental difference between electrolytes and

## 1. Introduction

Ion mobility is a critical performance parameter not only in electrochemical energy storage and conversion but also in other electrochemical devices. It is of particular importance in solid electrolytes and electrode materials. A thorough understanding of the basic principles underlying the ion mobility in crystalline materials is not only interesting from a fundamental, but also from an applied point of view<sup>[1]</sup> as, for example, the reduced performance of batteries at low temperatures is supposed to be related to low

electrodes: electrolytes are ion conductors, but they should be electronic insulators; otherwise, no electrons would flow through an outer circuit upon battery operation. Electrodes, on the other hand, should be both ion as well as electron conductors; otherwise, the recombination of ions and electrons upon entering electrodes would not be possible. Still, from a quantum chemical perspective, there is no fundamental difference in the determination of migration properties which crucially depend on the minimum energy path connecting two equivalent intercalation sites and the maximum activation barrier along this path.

The nature of the migrating species and the overall charge state are related topics that need to be discussed. Is the migrating species in solid electrolytes really an ion or rather an atom? We will address this issue by discussing various charge partition schemes which are supposed to determine the charge state of atoms in a chemical environment. A basic notion of macroscopic materials is that they are typically charge-neutral. This concept is well-known from liquid electrolytes where the charge of any solvated ion is compensated by a corresponding counter ion. Solid electrolytes are often coined "single-ion conductor." If these materials are single ion conductors, the natural question arises: What is the counter ion in these single ion materials? Furthermore, ion mobility might not just proceed via the hopping of single ions; there might also be concerted processes involved.

There is a wide class of different crystalline materials used in batteries such as spinels, perovskites, olivines, Prussian blue, NASICON, Chevrel phase, layered oxides, and van der Waals bonded layered systems. Apart from the structural differences of all these material classes, the interaction of the migrating ion with these different host lattices differs to a certain extent as


M. Sotoudeh, S. Baumgart, M. Dillenz, J. Döhn, K. Helmbrecht, D. Stottmeister, A. Groß

Institute of Theoretical Chemistry  
Ulm University  
89081 Ulm, Germany

E-mail: axel.gross@uni-ulm.de

K. Forster-Tonigold, A. Groß  
Helmholtz Institute Ulm (HIU)  
Electrochemical Energy Storage  
89081 Ulm, Germany

K. Forster-Tonigold  
Karlsruhe Institute of Technology (KIT)  
P.O. Box 3640, D-76021 Karlsruhe, Germany

 The ORCID identification number(s) for the author(s) of this article can be found under <https://doi.org/10.1002/aenm.202302550>

© 2023 The Authors. Advanced Energy Materials published by Wiley-VCH GmbH. This is an open access article under the terms of the Creative Commons Attribution License, which permits use, distribution and reproduction in any medium, provided the original work is properly cited.

DOI: 10.1002/aenm.202302550

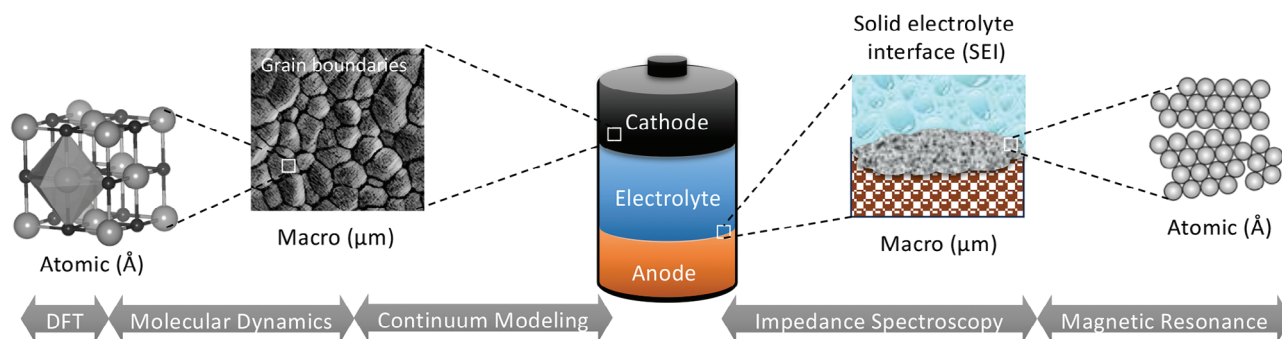


**Figure 1.** Schematic illustration of the relevant scales and configurations explored within a battery material. The methods utilized to calculate ion transport properties in the respective length scales are indicated by gray arrows, namely density functional theory (DFT) and molecular dynamics (MD) simulations. The experimental techniques employed to directly probe ion transport are also aligned with their corresponding length scales.<sup>[6]</sup> The figure illustrates the diverse range of scales, from atomic to mesoscale, and the corresponding configurations occurring in a battery. Investigating battery materials in such a way will lead to improved performance characteristics for future battery generation.

well. Hence, we will dedicate a full section to each of these material classes.

A very helpful tool to understand the principles underlying material properties is the descriptor concept, which can be regarded as the relation between desired or undesired features such as the ion mobility with basic material properties. Once such a descriptor has been successfully established, the search for materials with desired functional properties can be significantly facilitated as there is no longer the need to perform numerous time-consuming experiments or numerically challenging quantum chemical calculations. However, identifying descriptors can not be fully separated from the fundamental issues discussed above as the very existence of a descriptor already reflects the presence of a fundamental principle underlying the existence of this descriptor.

## 2. Obstacles for Ion Mobility within Crystals

In this review, we concentrate on the ion mobility in single crystals. Still, macroscopic solid materials are typically not single crystals but have a fine structure. There are further structural factors that might influence the ion mobility.

- **Electrochemical reactions at the interfaces:** In battery systems, crystalline materials interface with other components such as the electrolyte, as shown in **Figure 1**. Unfavorable interfacial reactions, such as the formation of a passivation layer or a high interfacial resistance, can impede ionic transport across the interfaces, resulting in a reduced battery performance.
- **Grain boundaries:** Polycrystalline materials, as employed in batteries, contain grain boundaries, which can act as barriers for ion migration, as schematically shown in Figure 1. These boundaries can also impede ion mobility and increase resistance to ion transport, limiting the overall performance and stability of the battery. Controlling and minimizing these boundaries is crucial for improving ion mobility. Note that the formation energies of point defects in the grain boundary are lower compared to the bulk lattice. Vacancies and interstitials have similar formation energies, indicating their equal importance in grain-boundary diffusion. Additionally, the diffusion anisotropy is influenced by the grain-boundary structure, with

faster or slower diffusion occurring along the tilt axis in tilt boundaries compared to diffusion normal to the tilt axis.

- **Defects and impurities:** Crystal defects, such as vacancies or interstitials, can disrupt the regular lattice structure and hinder or facilitate ion mobility. Additionally, impurities or dopants present in the crystal can alter the electronic properties and affect the mobility of ions.
- **Anisotropic diffusion:** Crystalline materials often exhibit anisotropic diffusion, meaning that ion mobility may vary significantly along different crystallographic directions. This anisotropy can result in an uneven distribution of charge carriers and lead to localized regions of high current density, which can promote side reactions, electrolyte decomposition, and even structural degradation of the material.
- **Structural constraints:** Crystal lattice constraints restrict the movement of ions within the material. The fixed crystal lattice can hinder the diffusion of ions, leading to lower ion mobility. This can result in slower charge/discharge rates and reduced overall battery performance.

Addressing these challenges requires a combination of materials design, synthesis techniques, and understanding of the fundamental mechanisms governing ion transport in crystalline materials. Strategies such as doping, nanostructuring, and interface engineering can be employed to enhance the ion mobility and improve the performance of crystalline materials in batteries. Still, it should be noted that typically the properties within the crystalline parts of a macroscopic material represent an upper bound for the ion mobility. Hence, a material which already has a low ion mobility as a single crystal should be disregarded as a promising material with respect to its migration properties.

## 3. Fundamental Mechanisms of Ion Mobility

In a crystal, the collective displacement of an atom is caused by numerous individual jumps of specific length. Fundamentally, an atom undergoes movement towards an adjacent location, which can either be a neighboring vacancy or an interstitial site. It is evident that the moving atom must navigate through the intervening lattice atoms, requiring energy to overcome activation barriers along the migration path which necessitates energy for

this process. Typically, the energy needed to activate the jump is considerably greater than the thermal energy  $k_B T$ .

At finite temperatures, atoms within a crystal oscillate around their equilibrium positions. Usually, these oscillations lack the necessary intensity to overcome the barrier, causing the atom to revert back to its original position. Occasionally, substantial displacements occur, resulting in a successful diffusion event of the atom. These occurrences of activation are infrequent compared to the frequencies of the lattice vibrations, which are characterized by the Debye frequency, typically ranging from  $10^{12}$  to  $10^{13} \text{ s}^{-1}$ . Once an atom has moved due to an activation event, the energy dissipates quickly. Consequently, the atom becomes deactivated and awaits many lattice vibrations on average before it jumps again. In a crystal, atoms undergo thermally activated motion, transitioning between lattice sites (or interstitial sites) through a sequence of distinct jumps.

The concept of atomic movement between neighboring sites was initially proposed by Wert,<sup>[7]</sup> and has since been further developed by Vineyard.<sup>[8]</sup> Vineyard's method builds upon the canonical ensemble of statistical mechanics, which considers the distribution of atomic positions and velocities. The process of an atomic jump can be understood as taking place within an energy landscape defined by the disparity in Gibbs free energy ( $G^{\text{migr}}$ ) between the saddle-point barrier and the equilibrium position. Here,  $G^{\text{migr}}$  represents the Gibbs free energy of atom migration (denoted as superscript *migr*) and can be divided into

$$G^{\text{migr}} = H^{\text{migr}} - T S^{\text{migr}} \quad (1)$$

where  $H^{\text{migr}}$  represents the enthalpy associated with the migration, while  $S^{\text{migr}}$  represents the entropy related to the migration. Through the application of statistical thermodynamics, Vineyard<sup>[8]</sup> demonstrated that the jump rate ( $\omega$ ), which signifies the number of jumps per unit time to an adjacent site, can be expressed as

$$\omega = \nu^0 \exp\left(-\frac{G^{\text{migr}}}{k_B T}\right) = \nu^0 \exp\left(\frac{S^{\text{migr}}}{k_B T}\right) \exp\left(-\frac{H^{\text{migr}}}{k_B T}\right) \quad (2)$$

The attempt frequency, denoted as  $\nu^0$ , is commonly referred to as the Debye frequency, which signifies the oscillation frequency occurring near the equilibrium position along the reaction pathway.  $k_B$  is the Boltzmann constant, and  $T$  denotes the absolute temperature. The entropy of migration signifies the alteration in lattice vibrations that accompany the displacement of the jumping atom from its equilibrium state to the saddle point configuration. In the Vineyard approach, the probability of reaching the transition state is derived by comparing the configurational partition functions of the initial state and the transition state, while the rate of crossing is determined by the one-way forward flux at the transition state. The expression for the migration entropy, in harmonic approximation, is therefore given by:

$$S^{\text{migr}} = k_B \left[ \sum_{j=1}^{3N} \ln\left(\frac{h\nu_j}{k_B T}\right) - \sum_{j=1}^{3N-1} \ln\left(\frac{h\nu'_j}{k_B T}\right) \right] \quad (3)$$

The frequencies  $\nu_j$  represent the  $3N$  normal modes for vibrations around the equilibrium site, while the  $3N - 1$  frequencies  $\nu'_j$  cor-

respond to the vibrations at the saddle point perpendicular to the jump direction with the constrained motion.

The macroscopic diffusivity is then obtained from the barrier of the single diffusion event by transition state theory (rate theory).<sup>[9]</sup> Assuming  $h\nu \gg k_B T$ , the effective frequency  $\nu^* = \nu^0 \exp(S^{\text{migr}}/k_B T)$  in the Arrhenius expression is obtained from the ratio of the product of the  $3N$  normal frequencies of the entire crystal at the initial configuration of a transition to the product of the  $3N - 1$  normal frequencies of the crystal when it is constrained in a saddle point configuration:<sup>[8]</sup>

$$\omega = \frac{1}{2\pi} \frac{\prod_{j=1}^{3N} \nu_j}{\prod_{j=1}^{3N-1} \nu'_j} \exp\left(-\frac{H^{\text{migr}}}{k_B T}\right) = \nu^* \exp\left(-\frac{H^{\text{migr}}}{k_B T}\right) \quad (4)$$

On the macroscopic scale, the diffusion coefficient ( $D$ ) is described by Fick's first law of diffusion:

$$\vec{J} = -D \vec{\nabla} c \quad (5)$$

where  $\vec{J}$  is the diffusion flux, which is the amount of substance (e.g., ions) passing through a unit area per unit time, and  $D$  is the diffusion coefficient, representing the proportionality constant between the diffusion flux and the concentration gradient ( $\vec{\nabla} c$ ). The units of the diffusion coefficient are typically square units of length per unit time (e.g.,  $\text{cm}^2/\text{s}$  or  $\text{m}^2/\text{s}$ ). The diffusion coefficient is a measure of how quickly particles (atoms, or ions) move through a medium due to random thermal motion. It quantifies the rate at which particles spread out from areas of high concentration to areas of low concentration. It is important to realize that this chemical diffusion differs from the tracer or Einstein diffusion, which is due to thermal fluctuation. Only at low concentrations of the diffusing particles, the chemical and the tracer diffusion coefficients are the same.

Ionic conductivity, on the other hand, is a measure of how well a material conducts electric current through the movement of charged ions. It is an important property in the context of electrolytes, which are substances that can conduct electricity when dissolved in a solvent or when in a molten state. Ionic conductivity ( $\sigma$ ) is described as a product of the concentration of mobile ions  $c$ , the charge of the ions  $q$ , and the mobility  $\mu$  of the charge carrier:

$$\sigma = qc\mu \quad (6)$$

The unit of the ionic conductivity is typically Siemens per meter ( $\text{S m}^{-1}$ ). Note that the diffusion coefficient at low particle densities relates to the movement of particles in a medium due to random motion, while ionic conductivity refers specifically to the ability of a material to conduct electric current through the movement of charged ions. Both properties are important in understanding ionic transport and are relevant in different scientific and technological applications.

The thermal dependency of the ionic conductivity is given by:

$$\sigma = \frac{\sigma_0}{k_B T} \exp\left(-\frac{H^{\text{migr}}}{k_B T}\right) \approx \frac{\sigma_0}{k_B T} \exp\left(-\frac{E_a}{k_B T}\right) \quad (7)$$

where the pre-exponential factor  $\sigma_0$  accounts for the entropy of migration, the jump distance, the attempt frequency, and a factor depending on the reaction mechanism. The height of the activation barrier is given by  $E_a$ . Besides, if non-interacting charge carriers are considered, the ionic conductivity can be expressed in terms of the diffusion coefficient  $D$ , by employing the well-known Nernst–Einstein relationship

$$D = \frac{\sigma}{cq^2} H_r k_B T \quad (8)$$

where  $H_r$  is the Haven ratio, which depends on the specific diffusion mechanism. It should be noted that in the presence of particle correlations, the behavior of individual particles significantly differs from the motion of the center of mass. Consequently, the conventional Nernst–Einstein equation is unsuitable, necessitating the utilization of a more precise formula derived from linear response theory to assess ionic conductivity.<sup>[10]</sup> This phenomenon must be considered when optimizing materials for practical applications. Recently, a substantial breakdown of the Nernst–Einstein relation in the diffusion and electromigration of  $K^+$  ions within single-walled carbon nanotube porins (CNTPs) with a diameter of 0.8 nm has been reported.<sup>[11]</sup> Molecular dynamics (MD) simulations with polarizable force fields unveil the disintegration of the water chain when subjected to electric fields, resulting in the formation of distinct  $K^+$ -water clusters that rapidly traverse the CNTP. Furthermore, it is shown that while individual ion-water clusters still adhere to the Nernst–Einstein relation, the overall relationship breaks down due to two separate mechanisms governing ion diffusion and electromigration.

Defects within crystalline solids can exhibit a strong impact on the ionic conductivity of the material. In 1926, the pioneering work of the Russian scientist Frenkel<sup>[12]</sup> marked the introduction of the point defect concept. Frenkel proposed that the movement caused by thermal agitation leads to atom transitions from their regular lattice positions to interstitial sites, resulting in the creation of lattice vacancies. This phenomenon is now known as Frenkel defect, which already encompassed the notions of vacancies and self-interstitials. In the early 1930s, Wagner and Schottky<sup>[13]</sup> expanded on this idea by investigating the general occurrence of disorder in binary AB compounds, considering the presence of vacancies, self-interstitials, and defects where atoms occupy the wrong sublattices.

The periodicity of the lattice in a defect-free crystal determines the mass and charge density. However, the introduction of a point defect disrupts this regular pattern. In metals, the presence of conduction electrons enables effective electronic screening of defects, resulting in uncharged point defects. Conversely, in ionic crystals, the formation of a point defect, such as a vacancy in one sublattice, disturbs the overall charge neutrality. To maintain charge balance, defect populations in ionic crystals can exhibit Frenkel disorder or Schottky disorder. Frenkel disorder involves an equal number of vacancies and self-interstitials in one sublattice, while Schottky disorder entails an equal number of vacancies in both, the cation and anion sublattices. For instance, in compounds like NaCl, which consists of cations and anions with opposite charges of equal magnitude, the number of vacancies in each sublattice must be equal to ensure charge neutrality.

In semiconductors, point defects introduce energy levels within the band gap, and their charge state (neutral or ionized) depends on the position of the Fermi level. In the subsequent sections, we will first examine point defects in metals and ionic crystals before going on to semiconductors.

### 3.1. Metals

Point defects play a crucial role in the diffusion processes within crystalline solids. This significance stems from two primary characteristics. First, point defects possess the ability to traverse the crystal lattice and facilitate the diffusion of atoms, essentially acting as carriers for this process. Second, these defects exist in a state of thermal equilibrium. In a crystal without defects, the mass and charge density exhibit periodicity in accordance with the lattice structure. The introduction of a point defect disrupts this periodicity. In metals, the conduction electrons effectively screen defects, resulting in uncharged point defects within the metal.

Diffusion in metals occurs when individual atoms or ions move from one location to another within the metal's crystal lattice, involving the movement of atoms from lattice sites to nearby vacant sites as well as migrating into interstitial sites between existing lattice atoms.<sup>[14]</sup> This process happens due to thermal energy, which causes the atoms or ions to vibrate. When atoms gain sufficient energy, they can overcome the forces holding them in place and move to neighboring lattice sites. The diffusion of atoms in metals is influenced by various factors, including temperature, concentration gradients, and the presence of defects in the crystal lattice.<sup>[15]</sup> At higher temperatures, atoms have more thermal energy, leading to increased diffusion rates. Concentration gradients also drive diffusion, as atoms tend to move from regions of higher concentration to regions of lower concentration to achieve a more uniform distribution. Diffusion in metals plays a crucial role in determining material properties, such as hardness, electrical conductivity, and corrosion resistance. For metal anodes in batteries, it should be mentioned that there is no mobility needed as the metal anode is either formed or dissolved upon charging or discharging, respectively.

### 3.2. Ionic Compounds

Ionic compounds, such as alkali halides, exhibit a fixed stoichiometry and possess a broad band-gap, rendering thermally generated electrons or holes negligible. These materials represent the traditional group of ion conductors, where conductivity originates from the existence and movement of vacancies and/or self-interstitials. A well-known example is silver iodide, for which fast ionic conduction was reported in 1914.<sup>[16]</sup>

In an ionic crystal, there is a limitation on the type and quantity of defects that can arise, as they require an equal count of cation and anion atoms in their structure. Subsequently, only defect populations that maintain charge neutrality can emerge. Furthermore, there is no need to take into account the formation of antisite defects, given the substantial Coulomb energy required for an ion to be situated in the incorrect sublattice.

Suppose the formation of vacancies and self-interstitials in the sublattice, arising from cations occupying cation sites. This

particular disorder is referred to as Frenkel disorder. Frenkel pairs are used to denote the combination of vacancies and self-interstitials. For undoped crystals to maintain charge neutrality, it is necessary for the quantities of vacancies and self-interstitials to be balanced and equal. The occurrence of Frenkel disorder can be observed within the silver sublattices of both silver chloride and silver bromide.<sup>[17,18]</sup>

Schottky disorder occurs when an equal number of vacancies are formed in both sublattices. In an undoped crystal, maintaining charge neutrality necessitates having equivalent concentrations of cation and anion vacancies. In the majority of alkali halides and numerous oxides, it has been observed that Schottky disorder is the primary factor influencing the distribution of defects.

### 3.3. Semiconductors

Semiconductor crystals provide a larger volume for the presence of self-interstitials compared to densely packed ionic structures. The formation enthalpies of vacancies and self-interstitials in semiconductors exhibit similar values. In the case of silicon, both self-interstitials and vacancies coexist in a state of thermal equilibrium and play significant roles in self-diffusion and solute diffusion processes. Conversely, in germanium, vacancies take precedence in thermal equilibrium and seem to be the sole defect relevant to the diffusion. Semiconductors can possess either neutral point defects or defects in different electronic charge states, as these defects create energy levels within the band-gap of the semiconductor. The neutrality or ionization of a defect is determined by the position of the Fermi level. A considerable dopant concentration significantly influences the diffusion process in semiconductors by utilizing defects with different charge states as carriers for diffusion. At lower temperatures, the impact of doping on diffusion becomes more noticeable as the intrinsic carrier density becomes exponentially suppressed upon lowering the temperature.

### 3.4. Crystalline Electrodes versus Crystalline Electrolytes in Batteries

So far, we have explored the intricacies of ion movement in solids, highlighting their behavior and interactions. These mechanisms are essential in the operation of various energy storage devices, such as batteries and supercapacitors. When ions migrate within a solid-state battery and cross electrode/electrolyte interfaces, they undergo redox reactions that result in the exchange of electrons. This electron flow, crucial for the energy transfer, generates an electrical potential difference between the electrodes, which is responsible for the cell's voltage.<sup>[19]</sup> Moreover, the rate and ease of ion migration, often determined by the choice of materials, crystal structures, and temperature conditions, significantly influence the cell's capacity and its ability to store and deliver electrical energy efficiently. Therefore, understanding and controlling the ion migration mechanisms in solid substances are fundamental aspects of electrochemistry, enabling the design of high-performance electrochemical cells for diverse applications, from portable electronics to renewable energy storage solutions.

In the following, we will unravel the complexities of these ion migration mechanisms within crystalline battery materials, recognizing their overarching influence on the electrochemical landscape.

In chemical and electrochemical systems, a reaction mechanism can occur in which guest species are inserted into typically vacant interstitial spaces within the crystal structure of a stable host material. This is particularly true for the electrodes, but to a certain extent also for solid electrolytes. While this insertion can significantly alter the chemical composition of the original host phase, in so-called insertion materials, it does not result in a change in its fundamental identity, the underlying crystal structure, or the proportions of the phases in the microstructure. In most cases, however, the addition of interstitial species to the previously unoccupied sites in the structure results in a change in volume that introduces mechanical stress and mechanical energy. The mechanical energy associated with the insertion and removal of interstitial species plays a central role in the hysteresis and subsequent energy loss observed in numerous reversible battery electrode reactions. In specific cases where species are inserted into materials with layered crystal structures, these insertion reactions are sometimes referred to as intercalation reactions. Reactions in which the composition of an existing phase is altered by the incorporation of guest species can also be considered as guest integration into the host material leading to a conversion of this material, and these processes are sometimes referred to as solid solution reactions.

In electrodes, the insertion of the “ions” = atoms occurs under conditions in which this insertion is thermodynamically favorable, playing a crucial role in determining the voltages and capacities of electrochemical cells. Often, when talking about electrolytes, it is assumed that they are liquids. However, it is worth noting that there are also various solid materials capable of fulfilling the main functions of an electrolyte. These solids enable the movement of charged ionic species while selectively impeding the transport of electronic species. Although there are numerous materials that effectively insulate against electronic currents, what sets apart materials capable of acting as a solid electrolyte is the high mobility of ionic species within their crystal structures.

AgI was one of the first solid-state ion conductors to exhibit high ionic conductivity. It was followed by the development of sodium-ion-conducting  $\beta$ -alumina and NASICON, and later, several fast lithium-ion conductors were discovered. Recent studies suggest that divalent cations, such as  $Mg^{2+}$  in mixed electron- and ion-conducting  $Mg_xMo_6X_8$  ( $X = S$  or  $Se$ ) (see Section 5.6) and ion-conducting metal borohydrides like  $LiBH_4 \cdot CH_3NH_2$ <sup>[20]</sup> or  $Mg(BH_4)_2 \cdot (NH_3)$ <sup>[21]</sup> can demonstrate reasonable mobility in solids. In the latter structures, the metal is coordinated by four borohydride complexes containing  $BH_4^-$  bridges between two metal atoms. Additional neutral molecules like  $NH_3$  or  $CH_3-NH_2$  can be introduced to interrupt the metal and  $BH_4^-$  network by forming  $N-H^{\delta+} \dots ^{-\delta}H-B$  dihydrogen bonds to interlink the remaining  $-BH_4-Mg-BH_4-$  chains. Furthermore, various anionic species can exhibit mobility in halides and oxides, such as oxygen-ion conductors at elevated temperatures. The polyhedral network comprises numerous metal and nonmetal ions, with chalcogens, halogens, and nitrogen serving as ligands. Polyhedra composed of early transition-metal ions from the first and second rows, such as  $Ti^{4+}$ ,  $Zr^{4+}$ ,  $Nb^{5+}$ , or  $Ta^{5+}$ , along with ions

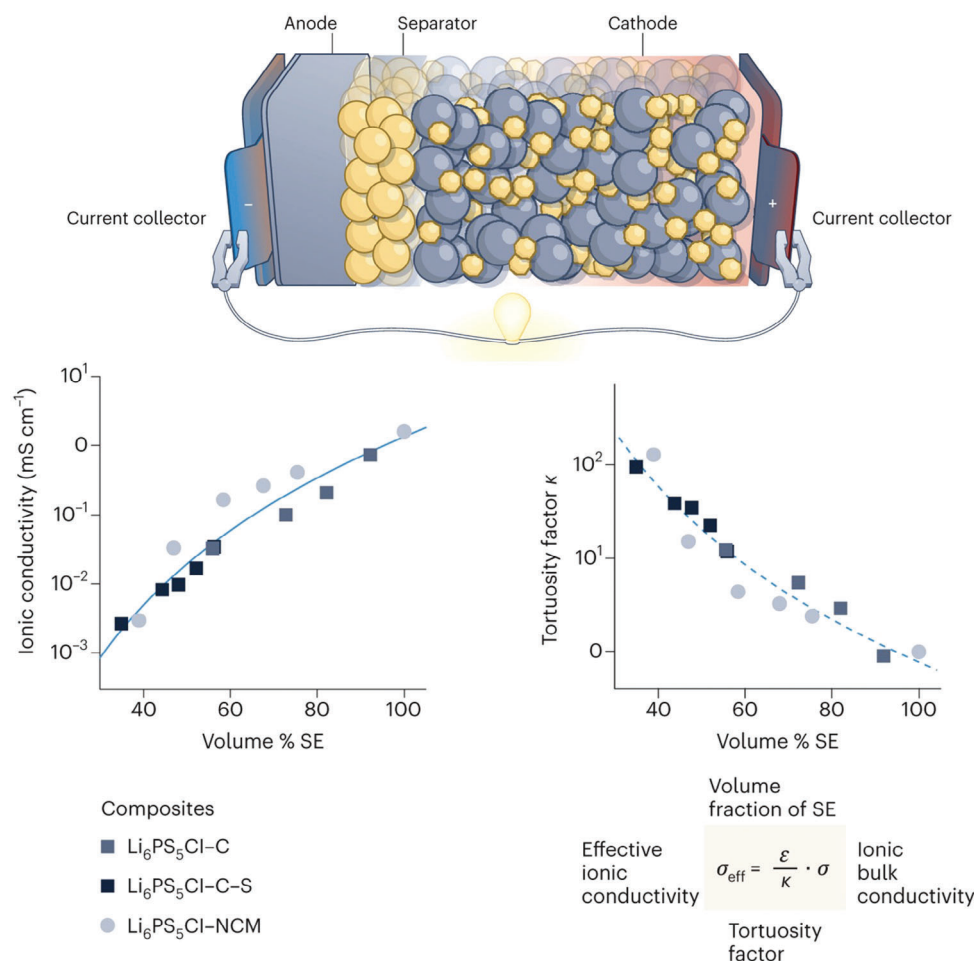


**Figure 2.** Schematic illustration of the generalized lithium solid-state battery (SSB) cell concept. Bottom graphs show the analysis of the partial lithium-ion conductivity ( $\sigma_{eff}$ ) and the assessment of the tortuosity factor ( $\kappa$ ) based on the weight fraction of the solid electrolyte (SE), which correlates with the volume fraction ( $\epsilon$ ). Reprinted with permission.<sup>[22]</sup> Copyright 2023 Springer Nature.

from groups 13, 14, and 15, are employed to form different coordination arrangements with the ligand. These polyhedra can form the backbone of the crystals in various configurations, such as isolated polyhedral units as seen in  $\gamma\text{-Li}_3\text{PO}_4$ , corner-sharing as in NASICON, or edge/corner-sharing as in garnets. The subsequent sections will provide further details on these ionic conductors.

Developing solid-state batteries (SSBs) requires thick cathode architectures and low solid electrolyte (SE) fractions in order to achieve high energy density, as illustrated in Figure 2. It has recently been demonstrated that reducing the volume fraction of the solid electrolyte in the composite significantly decreases the effective ionic conductivity of inorganic SEs compared to their bulk conductivity,<sup>[22]</sup> as shown in Figure 2. In addition, solid electrolytes need effective conductivities above  $10 \text{ mS cm}^{-1}$  to achieve fast rates in cathode composites. If completely solid cathodes cannot meet performance or long-term operation requirements, hybrid electrolytes or liquid electrolytes (LEs) may be employed, the so-called almost solid electrolytes. Lowering lithium content and finding less critical compositions in SEs, along with optimized composite route preparation, are crucial for SSBs to effectively

replace lithium-ion batteries (LIBs). Although considered safer, the increased safety of SSBs needs unequivocal proof, as there are potential safety risks associated with short circuits, toxic SEs, and percolation of the liquid electrolytes to the anode. Note that binaries are simple compounds that can be used as coating materials to prohibit electrolyte degradation. In particular, halides have been identified as suitable coating materials due to their favorable electrochemical stability together with exhibiting a suitable ionic mobility.<sup>[23–25]</sup>

Ternary materials such as inorganic oxides,<sup>[26,27]</sup> hydrides,<sup>[28–30]</sup> and chalcogenides<sup>[2,25,31–33]</sup> display commendable bulk ionic conductivities. Among these, chalcogenide spinel lattices have been recognized as ionic conductors with high ion mobility,<sup>[31,33]</sup> a crucial property for solid electrolytes. Spinel compounds, including transition metals like Cr and Mn, possess high binding energies<sup>[34]</sup> and satisfactory electron conductivity, rendering them appropriate cathode materials. Conversely, closed-shell systems like Sc and Y exhibit relatively low electron conductivity, qualifying them for use as solid electrolytes.<sup>[2,25,31]</sup>

Despite the wide electrochemical stability window (ESW) observed in many solid-state electrolytes (SSEs), several fast ion

conductors discovered so far remain unstable at low potentials when paired with negative electrodes like graphite and metallic lithium. This necessitates the use of alternative electrode materials like titanates. In addition, fast ion conductors can also react with positive electrode materials, leading to sluggish interfacial charge-transfer kinetics. The impact of volume changes has been also explored in various categories of solid electrolytes,<sup>[35]</sup> where enlarging the underlying lattice structure by substituting larger ions into the polyanion motive suppresses the rotational motion, which in turn promotes ionic conductivity of the materials. However, this phenomenon does not apply to  $\alpha$ -Li<sub>2</sub>SO<sub>4</sub> and  $\alpha$ -Na<sub>3</sub>PO<sub>4</sub>, which are part of a distinct group of inorganic ionic plastic crystal electrolytes. While the substitution of elements within a specific structural family can enhance ionic conductivity, there is a lack of comprehensive knowledge to establish a universal guide for fast ion conductors across various structural families. Consequently, predicting the most conductive structure/composition is challenging, impeding the design of new or multilayer ionic conductors that exhibit improved conductivity and stability, meeting the requirements of solid-state batteries. Therefore, further research is necessary to investigate trends and mechanisms in ionic conductivity among different classes of ion conductors. This will offer valuable insights into universal descriptors of ionic conductivity and facilitate the design of advanced ionic conductors.

### 3.5. Diffusion Mechanisms

The initial step in understanding atom diffusion within solids involves examining the various mechanisms of diffusion that come into play.

#### 3.5.1. Interstitial Mechanism

In materials allowing interstitial diffusion, migrating atoms can be incorporated into the interstitial sites of the host lattice to form a solid solution known as an interstitial solid solution. The interstitial sites are determined by the host lattice's geometry. In lattices such as fcc and bcc, the interstitial solutes typically occupy octahedral and/or tetrahedral interstitial sites. The diffusion of an interstitial solute occurs when it jumps from one interstitial site to an adjacent site. This mechanism is referred to as interstitial diffusion, as illustrated in **Figure 3**.

The migration path of an interstitial atom begins at an equilibrium position, from where the atom moves to the configuration known as the transition state (saddle point) where the lattice experiences maximum strain, as this is the energetically least favorable position along the migration path and then moves to a neighboring interstitial position. In the saddle-point configuration, the surrounding matrix atoms need to move aside to allow the passage for the migrating atom. Conceptually, this represents the most straightforward diffusion mechanism. It is alternatively referred to as the direct interstitial mechanism. Diffusion coefficients for atoms undergoing migration through the direct interstitial mechanism typically exhibit relatively high values because the interstitial atom does not have to wait for a defect to align in order to execute a jump. This mechanism is relevant for the migration of small atoms that can easily occupy interstitial posi-

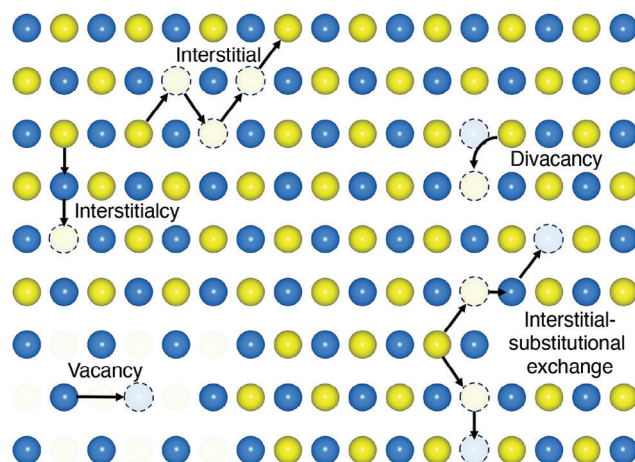


**Figure 3.** Schematic depiction of the different mechanisms of ion migration. The arrows illustrate five separate, common migration mechanisms: the vacancy mechanism (lower left), the direct interstitial mechanism (top left), interstitialcy mechanism (middle left), the divacancy mechanism (top right) representative of all multivacancy mechanisms, and the interstitial-substitutional exchange mechanism (bottom right). The circles represent framework atoms and charge carrier atoms in blue and yellow, respectively. Vacant sites are indicated by a dotted circle, while atoms that are faded out without any feature are marked as not existent.

tions and which do not significantly disturb the atoms of the host material from their normal lattice positions when they move.

#### 3.5.2. Vacancy Mechanism

In the vacancy mechanism, the propagation of an atom proceeds through migration along vacancy sites, as shown in **Figure 3**. This mechanism has been acknowledged as the primary means for the diffusion of matrix atoms and substitutional solutes in metals. Furthermore, its applicability extends to the diffusion phenomenon observed in various ionic crystals, ceramic substances, and even germanium. Nevertheless, some materials characterized by unique structures can attain elevated levels of ionic conductivity without requiring a high concentration of defects. These structures typically comprise two sublattices: a crystalline framework consisting of stationary ions and a sublattice housing mobile species. To achieve rapid ionic conduction in such structures, three essential criteria must be met: First, the number of equivalent (or nearly equivalent) sites accessible for the mobile ions to occupy should greatly exceed the count of mobile species; second, the migration barrier between the adjacent available sites should be sufficiently low to facilitate easy ion movement between them; and finally, these available sites must be interconnected to form an uninterrupted diffusion pathway.<sup>[36]</sup>

#### 3.5.3. Divacancy Mechanism

Diffusion can take place through clusters of vacancies, such as divacancies and trivacancies, as long as the formation of these agglomerates is energetically feasible, as illustrated in **Figure 3**. In thermal equilibrium, there is always a non-zero statistical probability that monovacancies meet and form divacancies. As

temperature increases, the concentrations of both mono- and divacancies at equilibrium also rise. However, the concentration of divacancies increases statistically more rapidly, thus becoming significant at high temperatures. In addition, divacancies in fcc metals exhibit greater mobility than monovacancies. Consequently, self-diffusion in fcc metals generally involves contributions from both the monovacancy and divacancy mechanisms. Apart from these differences, the two mechanisms strongly resemble each other. The influence of bound trivacancies on diffusion is usually considered negligible.

### 3.5.4. Interstitialcy Mechanism

Diffusion can take place through the interstitialcy mechanism, also known as the indirect interstitial mechanism, when an interstitial atom has approximately the same size as the lattice atoms or the lattice atoms within a specific sublattice of a compound. In this mechanism, a (self) interstitial atom replaces an atom located at a substitutional site, which in turn displaces a neighboring lattice atom, as illustrated in Figure 3. It is worth noting that non-collinear variations of the interstitialcy mechanism, where atoms move at an angle to each other, can also occur. These mechanisms are considered collective mechanisms because they involve the simultaneous movement of at least two atoms.

In metals, the contribution of the interstitialcy mechanism to thermal diffusion is insignificant. This is due to the relatively high formation enthalpies of self-interstitials when compared to vacancies. However, the interstitialcy mechanism plays a crucial role in radiation-induced diffusion. When a crystal is subjected to energetic particles such as protons, neutrons, or electrons, the atoms within the lattice are displaced from their original positions, resulting in vacancies. Simultaneously, the displaced atom becomes a self-interstitial as it is embedded back into the lattice. Consequently, pairs of vacancies and self-interstitials, known as Frenkel pairs, are created without thermal activation. Once these defects gain mobility, they facilitate diffusion and contribute to radiation-induced diffusion, which pertains to the study of crystal damage caused by radiation.

### 3.5.5. Interstitial–Substitutional Exchange Mechanisms

Solute atoms have the ability to dissolve in a solvent crystal on interstitial sites as well as substitutional sites. These solutes, known as “hybrid solutes,” can then undergo diffusion through interstitial–substitutional exchange mechanisms. Typically, the diffusivity of hybrid solutes in the interstitial arrangement is significantly greater than their diffusivity in the substitutional arrangement. Under such conditions, the incorporation of solute atoms can occur by fast diffusion of interstitial and subsequent change-over to substitutional sites, as shown in Figure 3.

Frank and Turnbull<sup>[37]</sup> originally suggested this mechanism to explain the fast diffusion of copper within germanium when the change-over involves vacancies. Subsequently, the diffusion of various foreign metallic elements in polyvalent metals like lead, titanium, and zirconium was also linked to this mechanism.

Rapid diffusion of gold (Au) in silicon was originally suggested by Gösele et al.<sup>[38,39]</sup> to occur through the change-over involv-

ing self-interstitials. Currently, this mechanism is also associated with the diffusion of other hybrid foreign elements like platinum, zinc in silicon, and zinc in gallium arsenide.

### 3.6. Concerted Migration

Concerted migration typically occurs when multiple ions move together as a group rather than individually. By this, the ions become more mobile and can move through the solid material more easily. This phenomenon is desirable because it can enhance the overall ionic conductivity of the solid material, enabling faster ion transport and thus improving the battery performance. It has already been demonstrated that similar phenomena significantly reduce the barriers of surface reactions when concerted reaction mechanisms are considered.<sup>[40]</sup> Nevertheless, such a concerted motion of the ions is not well described with conventional diffusion models. While a comprehensive understanding of the migration mechanism has been provided, predicting  $E_a = 0.5$  eV for  $\text{Li}_5\text{La}_3\text{Ta}_2\text{O}_{12}$  composition,<sup>[41]</sup> the conventional model falls short in capturing the phenomenon of superionic conduction in  $\text{Li}_7\text{La}_3\text{Zr}_2\text{O}_{12}$  ( $E_a = 0.3$  eV)<sup>[42]</sup> with the same crystal framework and comparable energy landscapes.<sup>[43]</sup>

During concerted migrations, the Nernst–Einstein equation fails to uphold the approximate correlation between the tracer diffusion coefficient and the ionic conductivity. As a substitute, the charge diffusion coefficient  $D_\sigma$  supersedes  $D_{tr}$ , and the accurate manifestation of the Nernst–Einstein equation yields the ionic conductivity as:

$$\sigma = \frac{Z_c^2 e^2 C}{k_B T} D_\sigma \quad (9)$$

where  $D_\sigma$  quantifies the diffusion behavior exhibited by the center of mass of the charge carriers,  $C = \frac{N_c}{V}$  represents the concentration of charge carriers in a given volume, and  $Z_c e$  signifies the magnitude of charge possessed by the carriers.

The charge diffusion coefficient, in contrast to the tracer diffusion coefficient, exhibits a direct proportionality to the ionic conductivity. The literature commonly denotes the ratio between the tracer and charge diffusion coefficients as the Haven ratio  $H_r = \frac{D_{tr}}{D_\sigma}$ . The reduction of the effective degrees of freedom due to the cooperativity of the Li ions exhibits a direct correlation with the Haven ratio, a widely recognized metric for elucidating the cooperative phenomena observed in ion conductors pertaining to ion dynamics.<sup>[44]</sup> The examination of the inequality<sup>[10]</sup> yielded valuable empirical knowledge regarding the distinction between the tracer and charge diffusion coefficients, resulting in hints for finding materials where the carrier-carrier interaction is long-ranged.

$$0 \leq D_\sigma \leq N_{eff} D_{tr} \quad (10)$$

In Equation (10),  $N_{eff}$  is an effective number of particles that the carrier can interact with in a given correlation time. Note that the correlations giving a large  $N_{eff}$  have a significant impact on the attempt frequency, assuming Arrhenius kinetics. However, these correlations do not influence the energy barriers involved in the process. This highlights the



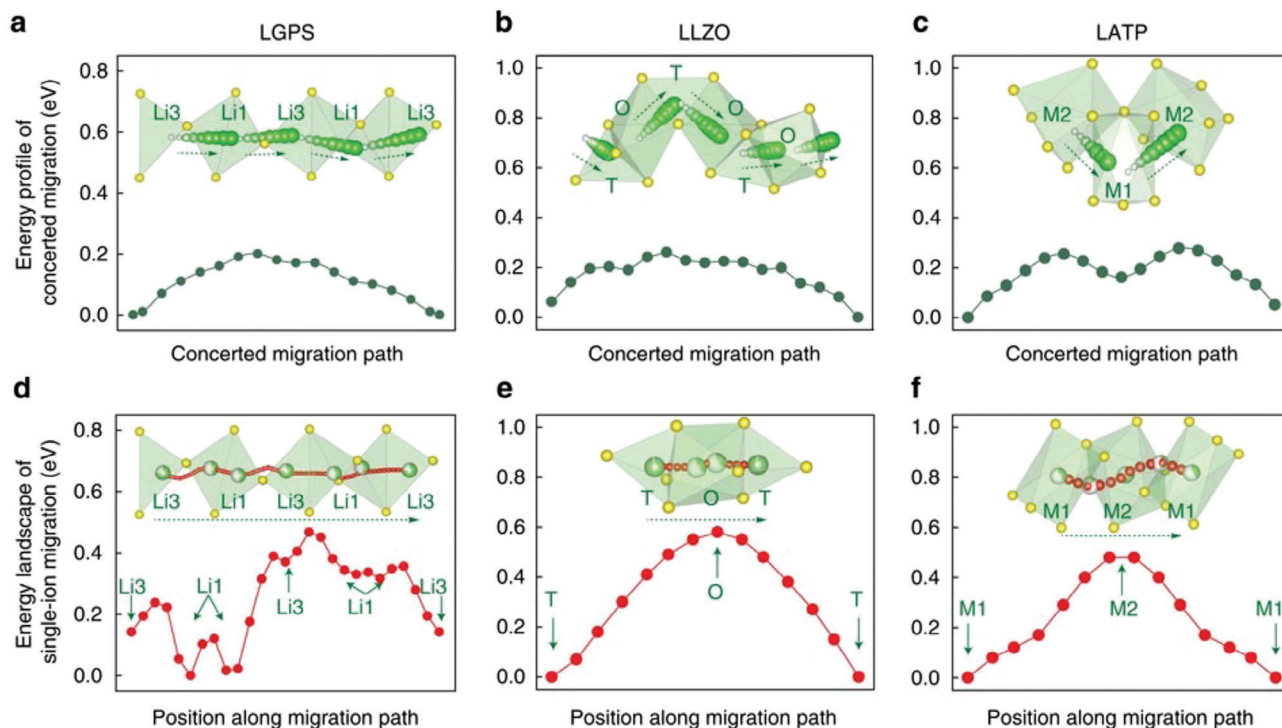


**Figure 4.** Energy barriers for collective migration of multiple Li ions in a)  $\text{Li}_{10}\text{GeP}_2\text{S}_{12}$  (LGPS), b)  $\text{Li}_7\text{La}_3\text{Zr}_2\text{O}_{12}$  (LLZO), and c)  $\text{Li}_{1.3}\text{Al}_{0.3}\text{Ti}_{1.7}(\text{PO}_4)_3$  (LATP), as they hop into adjacent sites along the diffusion channel. Insets depict the pathway of  $\text{Li}^+$  ions (represented by green spheres) and the surrounding O/S ions (represented by yellow spheres). d–f) Energy landscape of a single  $\text{Li}^+$  ion hopping along the migration channel (shown in the insets) spanning multiple Li sites (partially filled green sphere) and the pathway of  $\text{Li}^+$  ions (depicted as red spheres). Reproduced with permission.<sup>[43]</sup> Copyright 2017 Springer Nature.

improvement of the conductivity with the factors governing the attempt frequency<sup>[10]</sup> rather than the energy barriers in the given system.

In addition, collective modes can emerge in a system of ions moving within a single-particle potential energy surface.<sup>[45]</sup> When strong ion–ion interactions constrain the ions to be spaced apart in a manner inconsistent with the energy landscape, a smoother energy landscape is experienced by the group as a whole as not all moving ions can be at equivalent extrema of the potential energy surface at the same time. These collective modes, if formed and mobile, dominate transport statistically over individual ion hops due to their higher barriers. To achieve fast ion conduction, it is important to engineer a high intrinsic concentration of mobile carriers by inducing frustration, which breaks symmetries and maximizes geometric frustration in the sublattice. Frustration flattens the energy landscape, preventing the trapping of mobile carriers in deep energy minima and promoting the exploration of degenerate states within a narrow energy window, resulting in a high concentration of mobile charge carriers and high interstate transition rates.

The superionic conductivity of a variety of Li and Na solid electrolyte materials was therefore attributed to the concerted migration of charge carriers.<sup>[46,47]</sup> For example, a significant degree of cooperative charge carrier motion characterized by low Haven ratios  $H_r$  was identified in superionic conductors  $\text{Li}_{10}\text{GeP}_2\text{S}_{12}$  ( $H_r = 0.42$ )<sup>[10]</sup> and  $\text{Na}_{10}\text{GeP}_2\text{S}_{12}$  ( $H_r = 0.56$ ).<sup>[48]</sup> In a related

study, the superionic conductors  $\text{Li}_{10}\text{GeP}_2\text{S}_{12}$ ,  $\text{Li}_7\text{La}_3\text{Zr}_2\text{O}_{12}$ , and  $\text{Li}_{1.3}\text{Al}_{0.3}\text{Ti}_{1.7}(\text{PO}_4)_3$  were shown to exhibit concerted migration of  $\text{Li}^+$  based on AIMD simulations and the van Hove correlation function,<sup>[43]</sup> as shown in **Figure 4**. Moreover, promoting the occupation of high-energy sites in the structure was suggested to activate concerted migration. Based on a classical diffusion model and nudged elastic band (NEB) calculations, it was shown that diffusion barriers for the concerted migration of several  $\text{Li}^+$  were significantly reduced as opposed to the energy landscape for single-ion migration, constituting a design principle for novel superionic conductors. This was verified experimentally for a series of  $\text{Li}_{6+x}\text{Sb}_{1-x}\text{S}_5\text{I}$  ( $\text{M}=\text{Si}, \text{Ge}, \text{Sn}$ ) solid solutions in which partial substitution of  $\text{Si}^{4+}$  in  $\text{Sb}^{5+}$  sites and  $\text{Li}^+$  in the lattice leads to the population of high-energy interstitial sites.<sup>[49]</sup> The resulting disordered  $\text{Li}^+$  distribution was found to activate concerted migration and lead to reduced activation barriers. Hence,  $\text{Li}_{6.6}\text{Si}_{0.6}\text{Sb}_{0.4}\text{S}_5\text{I}$  was identified exhibiting superionic conductivity of  $14.8 \text{ mS cm}^{-1}$  and a low activation barrier of 0.25 eV. Concerted migration mechanisms are not only limited to Li and Na conductors; even for multivalent charge carriers, concerted migration can lead to increased ionic conductivity as recently illustrated in  $\text{Ca}_{1.5}\text{Ba}_{0.5}\text{Si}_5\text{O}_3\text{N}_6$ .<sup>[50]</sup> In this material, static vacancy configurations were found to enable 1D diffusion pathways leading to temporary occupation of nearest-neighbor Ca sites. In these Ca configurations, significant interactions of mobile ions resulted in the activation of a “vacancy-adjacent” concerted migration mechanism.

### 3.7. Charge Analysis

The term “ion mobility” suggests that *ions* are moving through the host material. However, the question arises whether ions really move as there is no unique way to associate charge to a particular atom in an extended material. Consequently, partial charges are typically associated with single atoms. While the concept of partial charges is frequently used in chemistry to gain an understanding of processes and reactions, an accurate quantum mechanical description, in the sense of a single observable, of atoms in molecules, is not possible. As a consequence, atomic partial charges have been described as “unicorns” before,<sup>[51]</sup> while Cho et al.<sup>[52]</sup> recently suggested the term “proxy variable” to be more appropriate. Regardless of the correct terminology, “atoms in molecules” (AIM) as a concept remains a somewhat arbitrarily human-defined tool. Nevertheless, many well-established mechanisms, like nucleophilic and electrophilic attacks in reactions, atomic electronegativities, or oxidation states in metalorganic compounds, rely on this idea of an existing charge partition. There is, therefore, a substantial demand for charge partition schemes to allow QM calculations to establish a proper connection to these concepts. All such methods must divide and allocate the existing charges to their respective atoms. This division can be done in two ways: by a sharp separation of real space where every atom is allocating a specific volume or by a softer partitioning where atomic volumes can overlap. It is essential to highlight that neither of the two approaches is necessarily better than the other, and their usefulness relies heavily on the desired purpose. Many reviews, in particular within the molecular chemistry community, have addressed and discussed the variety of charge partitioning schemes available today.<sup>[53]</sup> While a comprehensive overview of the many different methods is far beyond the scope of this paper, we nonetheless wish to introduce some of the most common schemes with a focus on their implementations within the field of ion mobility in crystalline battery materials.

The Bader charge analysis method is among the most used charge partition schemes and falls into the first sharp real space division category. Using Bader et al.’s<sup>[54]</sup> pioneer work, which establishes a quantum theory of atoms in molecules, this scheme analyses the charge density and divides the real space along minima in the charge density. Bader charges are used to partition the electron density within many material classes of particular interest for the development of batteries. In the case of spinels, the Bader charge analysis is frequently used to derive values for the oxidation states within the material.<sup>[55–58]</sup> The importance of the oxidation state with respect to the ion mobility has been shown for both perovskites,<sup>[59]</sup> as well as layered oxides,<sup>[60]</sup> where structures with increased ion mobility can be stabilized depending on the oxidation state of the transition metal. Pramanik et al.<sup>[61]</sup> used Bader charges to highlight the importance of the oxalate group in redox processes in their perovskite oxalate material. He et al.<sup>[62]</sup> utilized the Bader charge analysis to describe the lithium mobility in layered oxides. Sotoudeh et al.<sup>[3]</sup> introduced a new descriptor concept for the ion mobility in crystalline solids in which the charge carriers’ charge plays an important role. This concept was derived after they had previously shown, using Bader charge analysis, that the stability of ions in chalcogenide spinels can only be understood if deviations from a purely ionic interaction are taken into account.<sup>[2]</sup>

A representative of the soft partitioning category is the Mulliken charge analysis.<sup>[63]</sup> Akin to the linear combination of atomic orbitals technique, a population analysis is used to divide the system’s wave function into atomic orbitals, followed by a division of the atomic overlap population among the involved atoms.<sup>[63]</sup> Within Mulliken’s initial method, the overlap population is divided equally. Improvements to the classical Mulliken charge analysis have been developed, among others, by Löwdin et al. (Löwdin charges) and Montgomery et al. (MBS-Mulliken), both of which address the fundamental problem of the basis set dependence of Mulliken charges. Hammouri et al.<sup>[64]</sup> used Mulliken population analysis to show that the lower partial charge of titanium in their spinel improves the Mg mobility. In contrast, Yu et al.<sup>[65]</sup> used Mulliken charges to investigate the electronic conductivity at the interfaces of layered oxides and spinels.

Another member of the second category of partitioning schemes is the Hirshfeld method and its many variants.<sup>[66]</sup> The Hirshfeld method calculates the charge density difference between the charge density of the system and the non-interacting atomic charge densities. Then it divides the resulting deformation density via a sharing function based on the atom’s local contribution to the non-interacting atomic charge density. This distribution of the combined deformation density along a sharing function has earned the Hirshfeld method the nickname “stockholder” partition analysis. Xu et al.<sup>[67]</sup> used this method to show the influence of the anion charge on Li mobility within iodite-type compounds.

Closely related to the Hirshfeld method is the Voronoi deformation density (VDD),<sup>[68]</sup> where instead of weighting the deformation density via a sharing function, the deformation density is divided into the real space partitioning non-overlapping Voronoi cells, placing the method in the first category of charge partitioning schemes defined above.

While the different charge partition schemes tend to agree qualitatively,<sup>[69]</sup> the exact values may differ significantly. Ullah et al.<sup>[70]</sup> used multiple charge partition schemes to analyze the adsorption and mobility of alkali-ions on boron–arsenide and found values for lithium from +0.99e (Bader) to +0.18e (Mulliken). These discrepancies between the different methods are not surprising, as both Mulliken and Hirshfeld charges tend to underestimate charges,<sup>[71]</sup> while Bader charges are sometimes overestimated.<sup>[72]</sup> The choice of the charge partitioning scheme should therefore depend on the desired chemical property and an understanding of the system in question. Löwdin population analysis has been shown to yield chemically reasonable charges for a variety of Li and Na-based cathode materials,<sup>[73]</sup> while Bader charges can be used to derive oxidation states.<sup>[74]</sup> Last, the Hirshfeld method’s use of the deformation density leads to generally physically meaningful results for the charge transfer.<sup>[68]</sup> The exact value extracted from charge partitioning schemes should, however, always be handled with caution, and any comparison between charges determined by different methods should only be attempted with a solid understanding of the methodologies of the different schemes. These difficulties concerning the comparison of differently derived charges may complicate future machine learning attempts to find possible descriptors. These same discrepancies between the charge partitioning schemes make it difficult to identify the nature of the migrating charge carrier with regard to its ionicity. In order to resolve this question, the charge

of the migrating species in the transition state should be examined for a variety of compounds, where the Hirshfeld method is expected to yield the most reasonable results due to the fact that it derives charges based on the deformation density.

The choice of the charge partitioning scheme should, therefore, depend on the desired chemical property and an understanding of the system in question. Due to the tendency of Bader charges to overestimate the charges of a system, that is, to give a rather ionic picture of the system, the Bader charge analysis can be used to derive oxidation states,<sup>[74]</sup> which are in themselves a strictly ionic picture. In contrast, the Hirshfeld method is well suited to evaluate a charge transfer due to the evaluation of the deformation density rather than the whole charge density.<sup>[68]</sup> Generally, methods focusing on a charge density difference (like Hirshfeld and the Voronoi deformation density) are prime candidates to describe a shift in the charge density of a given system. Perhaps paradoxically, the most challenging property to evaluate is the physical charge of any given atom in a given system. Here, several factors can severely influence the usefulness of a charge analysis scheme, and one must ask: Is the material crystalline or amorphous? Is the system organic or inorganic? How localized are the electrons? For example, real space dividing schemes like VDD or Bader may yield reasonable charges for crystalline materials; however, such a scheme might associate rather unrealistic volumes with the respective nuclei for more amorphous materials. Further, wavefunction-based methods like Mulliken or Löwdin can be used to derive chemically reasonable charges for various Li and Na-based cathode materials<sup>[73]</sup>; however, depending on the electronic structure and the basis set, large overlap populations can be problematic to partition. The charge partitioning scheme choice is best made on a case-by-case basis for the physical charge. The exact value extracted from charge partitioning schemes should, however, always be handled with caution, and any comparison between charges determined by different methods should only be attempted with a solid understanding of the methodologies of the different schemes.

## 4. Accelerated Materials Discovery

### 4.1. General Remarks

Efficient ionic conductivity is a crucial factor for the development of high-performance batteries. In the pursuit of discovering materials with superior ionic conductivity, researchers are employing a combination of cutting-edge computational techniques and automated experimental investigations. This concerted approach aims to discover new compounds and explore alternative structural configurations that can support the swift movement of ions.

One promising avenue for materials discovery lies in the utilization of high-throughput computational techniques together with modern research management tools.<sup>[75]</sup> By leveraging the power of computational modeling and simulations, scientists can rapidly screen a vast array of potential compounds and identify those with desirable properties for ionic conductivity. This computational exploration provides valuable insights into the trends that govern ion mobility and helps to narrow down the list of candidate materials for further experimental validation.

The collaboration between computational and experimental studies is essential for verifying the predicted properties of candidate compounds. Experiments involving synthesis, characterization, and testing enable researchers to assess the actual performance of predicted materials and validate their ionic conductivity. This process allows for iterative refinement of computational models, leading to increasingly accurate predictions and a deeper understanding of the underlying principles governing ionic conduction.

In addition to modifying existing electrode materials that have shown promise in liquid-based batteries, researchers are actively exploring novel electrode materials and protective coatings tailored for solid-state battery applications. These materials must meet the stringent requirements of solid-state systems, including low and isotropic volumetric expansion during cycling.

By seeking electrode materials that exhibit low and isotropic volumetric expansion upon cycling, researchers aim to address one of the key challenges in solid-state battery technology. This feature allows for improved cycling stability and avoids the formation of cracks or delamination at the electrode-electrolyte interfaces. Consequently, the overall ionic conductivity of the battery system is enhanced, leading to superior performance in terms of energy density, lifespan, and safety.

Ultimately, the field of materials discovery for enhanced ionic conductivity is a dynamic and interdisciplinary area of research. By combining computational approaches with experimental investigations, scientists are continuously striving to identify new compounds and structural types that support fast ion conduction. Through exploring novel electrode materials and protective coatings, researchers are working toward the development of solid-state batteries with exceptional performance characteristics, bringing us closer to the realization of advanced energy storage technologies.

### 4.2. Descriptors and Design Principles

A highly valuable concept for expediting the process of discovering new materials relies on descriptors, as, for example, addressed by Ghiringelli et al.<sup>[76]</sup> and Isayev et al.<sup>[77]</sup> These descriptors encompass essential properties of materials or their combinations, which exhibit a correlation with the desired or undesired functionalities of the materials. This concept has demonstrated remarkable success in the field of heterogeneous catalysis, particularly in conjunction with scaling relations, as discussed by Nørskov et al.<sup>[78]</sup> and Man et al.,<sup>[79]</sup> and has already found applications in battery research, as indicated by Jaekle et al.<sup>[80]</sup> The identification of descriptors can significantly expedite the search for novel materials possessing the desired functional properties. Once identified, these descriptors can be optimized in the initial stages of the search for materials with improved properties, allowing the identification of promising candidate materials whose properties can be thoroughly examined.

With respect to solid-state ion mobility, several potential descriptors have been suggested, such as lattice volume and ionic size,<sup>[1,33]</sup> the selection of the anion sublattice,<sup>[1,81]</sup> lattice dynamics,<sup>[1,82,83]</sup> and the preferred crystal insertion site.<sup>[84]</sup> However, many of these identified descriptors are limited to specific

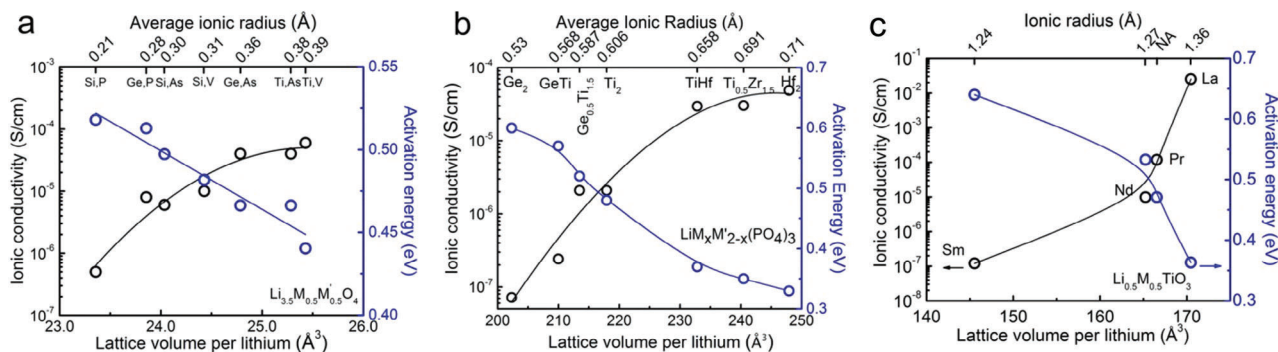


**Figure 5.** The graphs (a) and (b) present a comparison of lithium-ion conductivity in two distinct material systems, namely LISICON-like  $\text{Li}_{3.5}\text{M}_{0.5}\text{M}'_{0.5}\text{O}_4$  and NASICON-like  $\text{LiM}_x\text{M}'_{2-x}(\text{PO}_4)_3$ , at room temperature. The variation in cationic radii for these materials is examined in relation to the lattice volume per lithium atom. Additionally, panel (c) illustrates ionic conductivities at 400 K and their respective activation energies and the relation to the lattice volume per lithium atom in perovskites  $\text{Li}_{0.5}\text{M}_{0.5}\text{TiO}_3$ , featuring A-site rare-earth metal ions  $\text{M} = \text{Sm}, \text{Nd}, \text{Pr}, \text{and La}$ . It is worth noting that the average ionic radius is calculated using Shannon's radii, and cases where  $\text{Pr}^{3+}$  is in a 12-fold coordination and the atomic radius is not available, are indicated as "NA." Reprinted with permission.<sup>[1]</sup> Copyright 2016, American Chemical Society.

crystal structures, and some rely on properties that are not easily accessible.

When the ligand is altered by descending in the periodic table, specifically involving chalcogens or halogens, there is typically an increase in the ionic conductivity of monovalent cations. As the electronegativity of the ligand decreases, we anticipate weaker attractive forces between the ligand and the mobile cation. For instance, when the ligand shifts from  $\text{F}^-$  to  $\text{I}^-$ , the conductivity of  $\text{Ag}^+$  and  $\text{Li}^+$  experiences a substantial increase across various halides like  $\text{LiX}$  (where  $\text{X} = \text{F}, \text{Cl}, \text{Br}, \text{and I}$ ) and the olivine  $\text{Li}_2\text{ZnM}_4$  (with  $\text{M} = \text{Cl}, \text{Br}, \text{and I}$ ). Notably, the rising lithium-ion conductivity in halides from  $\text{LiF}$  to  $\text{LiI}$  can be associated with an increasing Li-X distance, greater halogen atom polarizability, and a reduced electronegativity of the halogen atom.

It is worth noting that the ionic conductivity of the lithium argyrodites family appears to deviate from this trend, as  $\text{Li}_6\text{PS}_5\text{I}$ , which should theoretically have the highest conductivity based on this trend, actually exhibits the lowest conductivity in the series. This seeming contradiction is attributed to the presence of sulfur anions in addition to halide anions within this family, with sulfur anions outnumbering halide anions by a 5-to-1 ratio per formula unit. Consequently, the  $\text{S}^{2-}$  ions are expected to exert a more substantial influence on ionic conductivity than the halide anions. Indeed, the conductivity of  $\text{Li}_6\text{PO}_5\text{Cl}$  is orders of magnitude lower than its sulfur-containing counterpart.

Expanding the lattice volume has the potential to enhance ionic conductivity and lower activation energy across various structural families. Enlarging the lattice volume for each lithium atom within a specific crystal structure results in heightened ionic conductivity and decreased activation energy for materials resembling LISICON (as depicted in Figure 5a), NASICON (as shown in Figure 5b), and perovskite (as illustrated in Figure 5c). It is noteworthy that in Figure 5b, the increase in lattice volume per lithium atom in NASICON-like  $\text{LiM}_x\text{M}'_{2-x}(\text{PO}_4)_3$  is associated with a greater bottleneck size for lithium ion diffusion. Furthermore, elevating the lattice volume by introducing larger A-site rare-earth metal ions (in the order  $\text{Sm} < \text{Nd} < \text{Pr} < \text{La}$ ) in the perovskite structure is linked to heightened lithium-ion conductivity and decreased activation energy.

Additionally, to provide a broad overview of the trends in migration energy barriers concerning the size of transition metals utilized in spinel materials, Figure 6 illustrates the relationship between migration energy and the ionic radii of B-cations.<sup>[25]</sup> The migration barrier was determined using the NEB method. Notably, a significant connection between the ionic radius of B-cations and the computed migration barriers is evident, with a distinct minimum observed in the range of 100 to 110 pm. This suggests heightened mobility of Mg-ions within this radius range. Consequently, the selection of the transition metal B can be employed to fine-tune ion mobility within spinel compounds.

Furthermore, the decrease in the frequency of the longitudinal optical mode ( $\omega_{\text{TO}}$ ) corresponds to a reduction in activation energy, which aligns with the concept that lower phonon frequencies are linked to greater vibrational amplitudes. Consequently, this enhances the likelihood of mobile species transitioning to adjacent lattice sites.<sup>[85]</sup> It is worth noting that a comparable correlation is observed between the enthalpy of migration and the frequency of longitudinal acoustic phonons at the 2/3 point along the [111] direction in the Brillouin zone for body-centered cubic metals.<sup>[86]</sup>

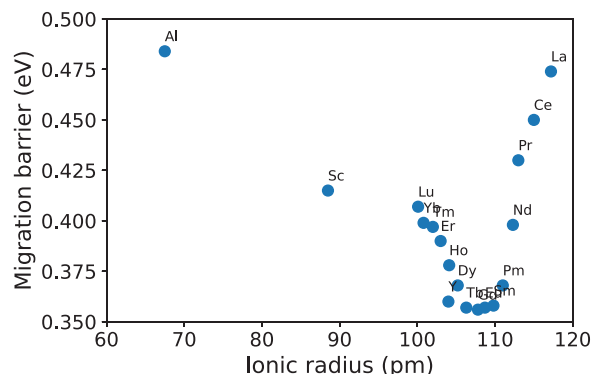


**Figure 6.** The relationship between migration barriers and the ionic radii of the transition metal cations in sulfide spinels is examined, with the calculated migration barriers presented in electronvolts (eV). Reprinted with permission.<sup>[25]</sup> Copyright 2022, American Chemical Society.

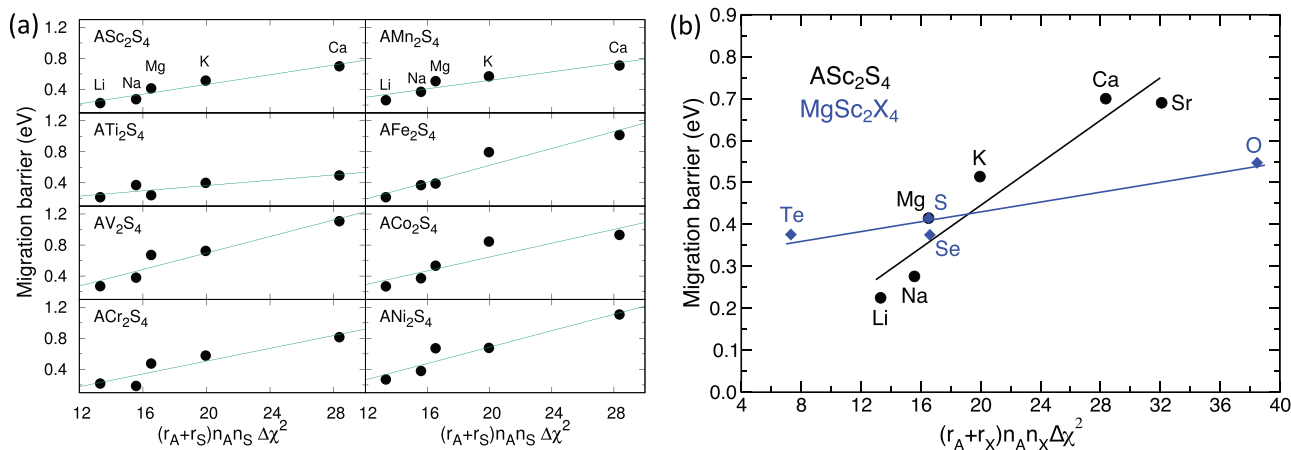


**Figure 7.** Migration barriers (in eV) in  $AB_2S_4$  spinels plotted as a function of the migration number  $N_{migr}$  for a) eight transition metal cations  $B = Sc, Ti, V, Cr, Mn, Fe, Co, Ni$ , while considering various migrating cations  $A = Mg, Na, K, Mg, Ca$ , and b) for  $ASc_2S_4$  (represented by black symbols) and  $MgSc_2X_4$  spinels (represented by blue symbols), including different monovalent and multivalent cations ( $A^{n+}$ ) and anions ( $X^{n-}$ ). Reprinted with permission.<sup>[3]</sup> Published under a CC BY license.

In 2022, Sotoudeh et al.<sup>[3]</sup> conducted first-principles electronic structure calculations to develop a descriptor for ion mobility in battery electrodes and solid electrolytes. This descriptor is composed of easily accessible observables, namely ionic radii, oxidation states, and Pauling electronegativities of the species involved. The study reveals that within a specific class of materials, the migration barriers can be related to this descriptor through linear scaling relations, as shown in **Figure 7**. These relations can be established by varying either the cation chemistry of the charge carriers or the anion chemistry of the host lattice. The existence of these scaling relations suggests that a purely ionic perspective is insufficient for understanding all the factors that influence the ion mobility in solid materials. The discovery of these scaling relations has significant implications as it shows the potential to accelerate the process of finding materials with desired ion mobility properties such as oxide spinels.<sup>[87]</sup> By utilizing this approach, researchers can more efficiently explore and identify

materials that exhibit enhanced ion mobility, thus contributing to the development of improved electrochemical devices, including batteries and solid electrolytes.

In further studies, machine learning (ML) was employed to measure the significance of various chemical, physical, and structural characteristics on the movement of ions within a crystalline lattice.<sup>[88]</sup> This work focused on the anti-perovskite crystal structure as a model system. Multiple ML algorithms were trained to predict ion migration barriers, using a dataset of over 600 barriers calculated consistently through density functional theory (DFT). The training set included 36 alkali metal chalcogenide anti-perovskites, encompassing vacancy and interstitial migration mechanisms (see **Figure 8**). Redundant features were identified and removed from the analysis to simplify the models and prevent overfitting. The most accurate algorithm was used to determine the feature combinations that yielded the most precise predictions. The study quantified the relative importance of features

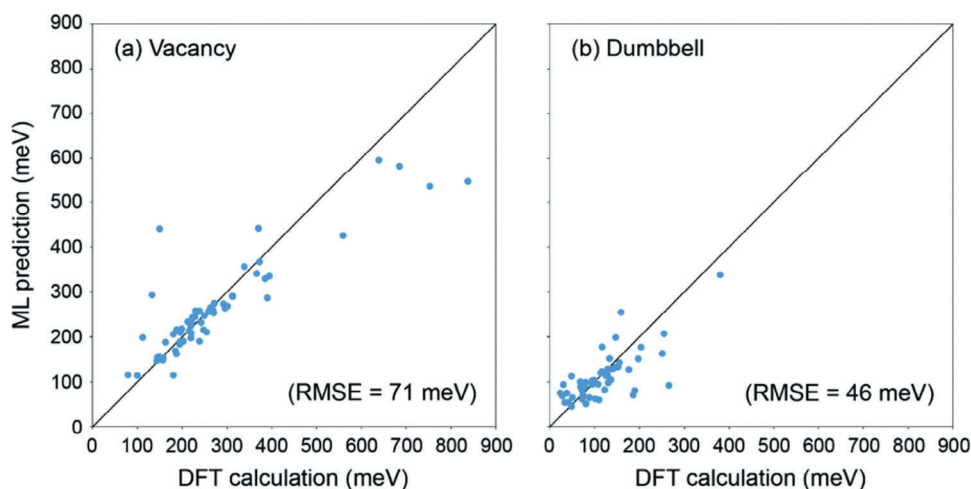


**Figure 8.** Comparing the effectiveness of the adaboost + ERTR ML model with DFT calculations, based on the best feature sets. a) Predicted vacancy migration barriers using five features, and b) predicted dumbbell migration barriers using three features. Reprinted with permission.<sup>[88]</sup> Copyright 2022, Royal Society of Chemistry.

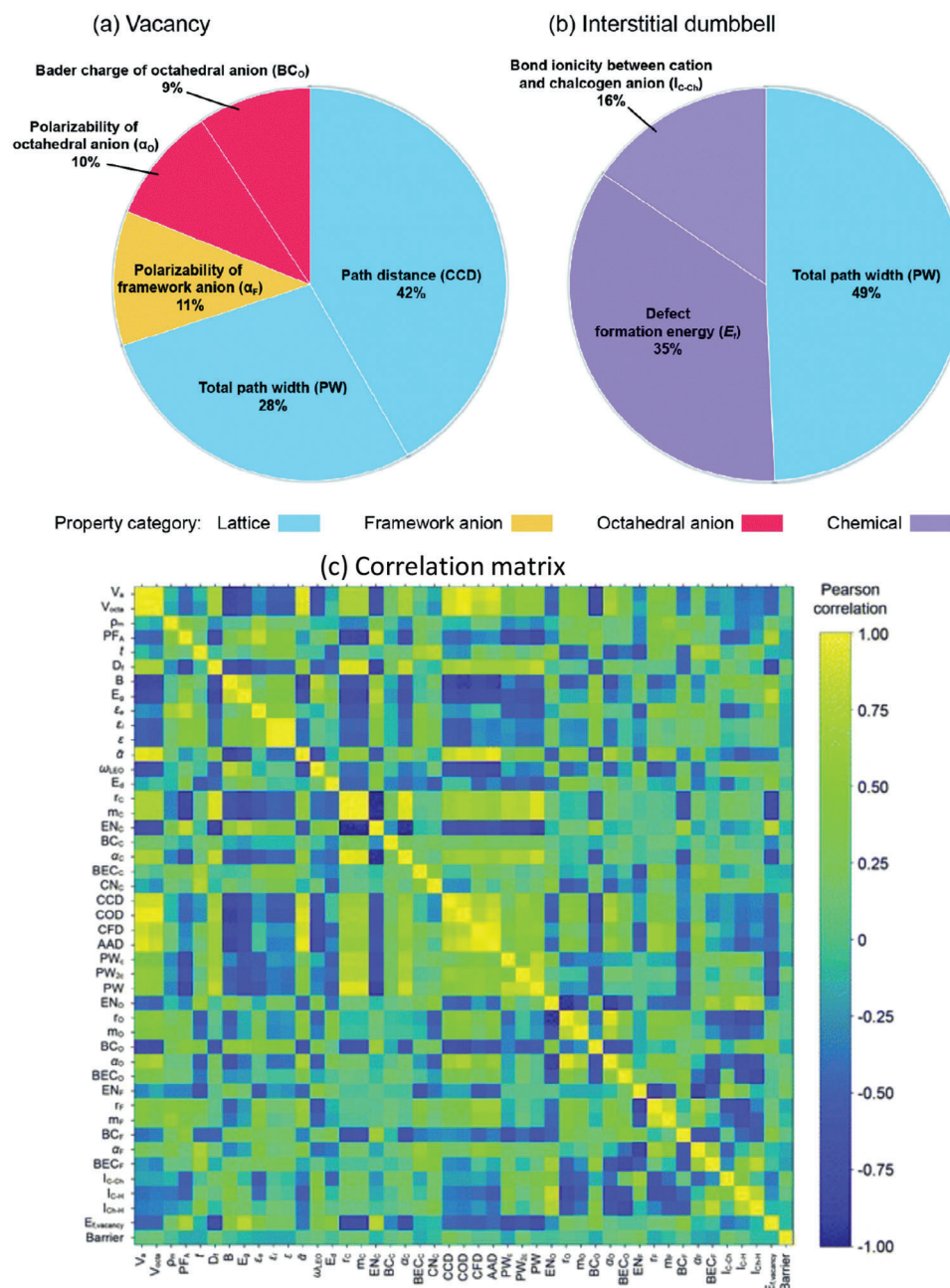


**Figure 9.** Assessing feature importance in ML models for ion migration through a) vacancy and b) interstitial mechanisms. Importance was measured using the mean decrease in impurity. c) The correlation between descriptors and vacancy migration barriers through Pearson correlation analysis. Reprinted with permission.<sup>[88]</sup> Copyright 2022, Royal Society of Chemistry.

and their influence on ion transport using mean decrease in impurity and individual conditional expectation (ICE) plots.

This analysis reaffirmed the significance of known mobility-influencing features, such as anion polarizability, and revealed the importance of other lesser-known factors. Notably, lattice properties like hopping distance and channel width were found to have the greatest impact on cation mobility. These features accounted for 70% of the feature importance in vacancy migration and for approximately 50% in interstitial migration, as illustrated in **Figure 9**. Analysis of these features using ICE showed that bar-

riers decrease as the hopping distance decreases and the channel width increases. Additional notable features included anion polarizability (22% for vacancy migration) and defect formation energy (35% for interstitial migration). The discovery of the defect formation energy as a significant feature for interstitial migration is noteworthy as it reflects a kind of Brønsted–Evans–Polanyi-type relation between activation energies and site preference of the charge carriers.<sup>[4]</sup>

Overall, these analyses will aid in designing efficient electrodes and solid electrolytes by narrowing down the essential properties

in a multidimensional design space. However, to extend the results beyond anti-perovskites, further research is necessary, such as incorporating dynamic phenomena like lattice vibrations and poly-anion rotations into the feature set. It is worth noting that the features used in this study for anti-perovskites can be readily evaluated for other types of crystalline conductors. Additionally, several important features identified here for vacancy migration have been discussed in literature for other crystal systems, indicating a potential transferability of these findings.

The olivine-type  $\text{LiMXO}_4$  chemical search space was effectively screened using the DFT+NN method.<sup>[89]</sup> The multi-output node architecture (diffusion barrier and cohesive energy) proved to be more accurate and interpretable compared to the single output node architecture and the partial least squares (PLS)-based method. Significantly improved predictions were observed for values near the extreme terminals of the attribute set (diffusion barrier and cohesive energy) compared to PLS-derived models. Incorporating a penalty term on the error function greatly reduced overfitting of the training data, resulting in a more robust model. Furthermore, utilizing literature-based multivariate input data showed promise for predicting target properties. The DFT data-based model (DN3) discovered candidate compositions such as  $\text{LiMgPO}_4$  (0.26 eV),  $\text{LiMgAsO}_4$  (0.17 eV),  $\text{LiScSiO}_4$  (0.29 eV), and several others, including compositions containing rare earth elements that were previously unidentified. The causal index (CI) sensitivity and variable importance in projection plots established the input–output relationships and relevance of input variables. For the DN3 model, descriptors of the local environment for the Li pass were found to be important input variables, whereas for the literature data-based neural network model, descriptors for the X cation played a crucial role. Techniques like CI plots and sensitivity profiles provided a systematic and unbiased way to interpret the models' underlying structure, but chemical reasoning is necessary to validate the input variables' relevance and identify potential issues arising from multicollinearity.

Jalen and colleagues<sup>[90]</sup> successfully developed an efficient and informative neural network-based functional for the composition space ofavorite  $\text{LiMTO}_4\text{F}$ , providing insights into the materials' magneto-electric (ME) properties. Among the potential solid electrolytes with ME values less than or equal to 0.30 eV, there are  $\text{LiGaPO}_4\text{F}$  (0.25 eV),  $\text{LiGdPO}_4\text{F}$  (0.30 eV),  $\text{LiDyPO}_4\text{F}$  (0.30 eV),  $\text{LiMgSO}_4\text{F}$  (0.21 eV), and  $\text{LiMgSeO}_4\text{F}$  (0.11 eV). By employing an informatics-based model along with chemical intuition, this approach helps to unravel the complex interplay of various parameters that influence the desired property, often in competition with each other. Key factors such as the size of the Li pathway bottleneck, polyanion covalency, and local lattice distortion were identified. Additionally, the study demonstrated the capability of predicting the target property (e.g., ME) for multiple structure types primarily using intrapolyhedron parameters.

Another model was developed to identify the parameters responsible for high Li-ion conductivity in garnet-structured oxides.<sup>[91]</sup> These parameters, mostly based on geometry, were derived from the relationships between constituent element radii and ion packing principles. The Li ion transport characteristics in garnet-structured oxides were analyzed using regression analysis (support vector regression—SVR), revealing the relationships between composition, structure, and ionic conductivity. Promising compositions were identified using t-stochastic triplet em-

bedding (t-STE), a method related to chemography or cartography in computer-aided molecular design. The models achieved a reasonable level of predictive ability, with the statistical parameters R-squared ( $R^2$ ), root mean squared error (RMSE), and mean absolute error (MAE) of the SVR model reaching 0.778, 0.372, and 0.283, respectively. The predictive errors were comparable to the variances in total conductivities reported in different publications. However, there are limitations to the model's predictive ability, which could be attributed to descriptor selection or intrinsic variance in the experimental data. The t-STE models demonstrated a clear allocation of chemical space areas based on the logarithm of total ionic conductivity ( $\log \sigma_{\text{tot}}$ ) values of compounds, confirming the suitability of the chosen descriptors for understanding composition–structure–property relationships. These models were used to evaluate  $\log \sigma_{\text{tot}}$  values for candidate compounds recommended for synthesis. Attempts were made to elucidate the relative site preferences of  $\text{Al}^{3+}$  and  $\text{Ga}^{3+}$  cations, focusing on compounds potentially unstable to moisture due to the accommodation of  $\text{Li}^+$  in tetrahedral and octahedral sites. However, the obtained results were inconclusive. Several candidate compounds have been recommended for synthesis as potential SSE materials.

Introducing a novel computational screening approach, Sendek et al.<sup>[92]</sup> presented a method for identifying potential SSE materials for LIBs. This approach allows to screen all known lithium-containing solids, tackling the challenge of simultaneously satisfying multiple requirements for high-performance electrolytes, which is challenging to achieve through experiments or computationally intensive ab-initio methods. Initially, they screened 12 831 crystalline solids with lithium content to identify structures possessing high structural and chemical stability, as well as low electronic conductivity and cost. Subsequently, they developed a data-driven model utilizing logistic regression to classify ionic conductivity, based on experimental measurements reported in the literature, thereby identifying candidate structures with fast lithium conduction. By employing this screening process, they narrowed down the list of candidates from 12 831 to 21 structures that exhibit promise as electrolytes, with only a few having undergone experimental examination. Interestingly, they found that individual atomistic descriptor functions lack predictive power for ionic conductivity; however, employing a multi-descriptor model proves to be useful. Furthermore, they observed that screening for structural stability, chemical stability, low electronic conductivity, and high ionic conductivity eliminates a significant portion of lithium-containing materials, reducing the list substantially. Notably, their screening approach capitalizes on structures and electronic information available in the Materials Project database.

A comprehensive database<sup>[93]</sup> has been published containing crystal structure information, ion migration channel connectivity data, and 3D channel maps for over 29 000 inorganic compounds. Currently, this database encompasses ionic transport properties for all potential cation and anion conductors, including  $\text{Li}^+$ ,  $\text{Na}^+$ ,  $\text{K}^+$ ,  $\text{Ag}^+$ ,  $\text{Cu}^{2+}$ ,  $\text{Mg}^{2+}$ ,  $\text{Zn}^{2+}$ ,  $\text{Ca}^{2+}$ ,  $\text{Al}^{3+}$ ,  $\text{F}^-$ , and  $\text{O}^{2-}$ , and this number is continually expanding. The methods employed for characterizing materials in the database involve a combination of structural geometric analysis based on Voronoi decomposition and bond valence site energy (BVSE) calculations, which provide information about interstitial sites, transport channels, and

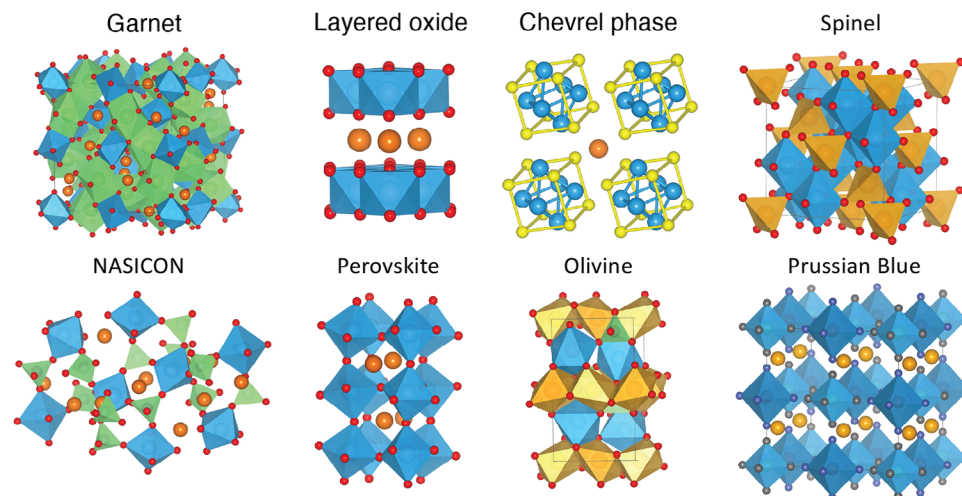


**Figure 10.** Supercells featuring the various crystal structures of materials considered in this study. The migrating ions are depicted with orange spheres or polyhedra, while the transition-metal ions are represented by blue octahedra. Green polyhedra symbolize the presence of polyanionic groups.

BVSE activation energy. The examples presented in this chapter demonstrate that accelerated materials discovery methods are increasingly used to derive trends in ion mobility. However, it is still not clear how general the observed trends are with respect to different materials classes, which will be discussed in the next section.

## 5. Materials Classes

In the following sections, we want to explore today's most important material classes of crystalline solids, which are researched for their use in battery technology. Still, the aim of this review is not a full account on all material classes since, unfortunately, covering all of them is far beyond the scope of this review. Therefore, we limited ourselves to the materials classes of spinels, olivines, garnets, perovskites, Prussian blue, Chevrel phase, layered oxides, NASICONs, halides, and anion migration systems. We are aware of the plethora of other materials out there, such as post-spinels,<sup>[94]</sup> weberites,<sup>[95]</sup> zircones,<sup>[96]</sup> borates,<sup>[97]</sup>  $V_2O_5$ ,<sup>[98]</sup> and  $\alpha$ - $MoO_3$ .<sup>[99,100]</sup>

### 5.1. Spinel

The spinel structure with a general formula  $AB_2X_4$  consists of a cubic close-packed arrangement of X atoms. In its conventional crystal structure, the A cations occupy 1/8 of the tetrahedral sites, while the B cations occupy 1/2 of the octahedral sites, as depicted in **Figure 10**. The B and X ions create a network of  $BO_6$  octahedra that share edges, while the A and O ions form a 3D network of tetrahedra that share corners. The A-type ions are relatively small, making their occupancy of the tetrahedral sites energetically more favorable than the occupation of the octahedral sites. The pyrochlore lattice is formed by the B ions, typically leading to pronounced geometric frustration effects. Along the [111] direction, two types of alternating stacking planes can be observed: a 2D triangular lattice and a kagomé lattice. The A sublattice of the

spinel structure assumes a diamond lattice shape. The presence of various competing factors, such as the crystal field stabilization of the transition metals (B cations) or entropic contributions, can give rise to a range of disordered or inverted configurations. In certain cases, a fraction of A cations, such as Mg, can swap places with the transition metal B cations, resulting in partially inverted lattices and charge disproportionation of the B cations ( $2B^{3+} \rightarrow B^{2+} + B^{4+}$ ).

At high temperatures, numerous spinels exhibit cubic symmetry; however, the presence of distorted  $BO_6$  octahedra cannot be dismissed. The octahedra undergo a trigonal distortion, leading to a transformation from  $O_h$  octahedral symmetry to  $D_{3h}$  octahedral symmetry.<sup>[2,87]</sup>

LIBs have effectively incorporated  $Mn_2O_4$  spinels into commercial applications as cathodes. Nevertheless, this specific spinel exhibits a significant obstacle to  $Mg^{2+}$  diffusion, with a barrier of 0.67 eV. This value surpasses the migration barriers for  $Li^+$  ions in all  $M_2O_4$  spinels (where  $M = Mn, Co, Ni, Cr$ ), which range from 0.40 to 0.60 eV.

The spinel structure possesses a desirable combination of capacity and voltage.<sup>[87]</sup> Recent studies<sup>[101,102]</sup> have reported experimental migration barriers of approximately 600 meV for  $Mg^{2+}$  in Cr- and Mn-spinel oxides, aligning with DFT calculations. It has been observed that structural disorder within the spinel lattice affects the migration of Mg ions, and this disorder can be regulated during synthesis. Nonetheless, the strong Coulombic interactions between the Mg cations and the oxide host lattice generally impede the reversibility of Mg intercalation and result in elevated Mg migration barriers. In addition, migration in the spinel structure is mediated by intermediate octahedral sites whose relative stability to the initial tetrahedral site, called site preference, strongly influences the resulting migration barriers.<sup>[84]</sup> In the ideal scenario in which the site preference tends toward zero, the activation barriers are minimized and any deviations toward higher or lower values result in an increased barrier. This observation can be inferred from the relationship between the activation barrier and the site preference, as depicted in **Figure 11**. As a result, this phenomenon presents potential avenues for



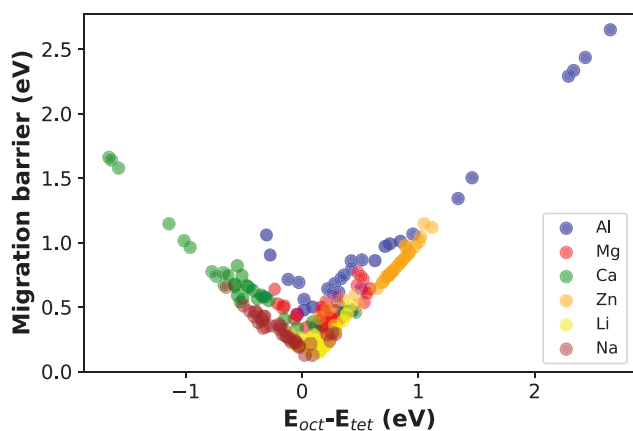


**Figure 11.** The migration barriers obtained from NEB calculations against the site preference  $E_{oct} - E_{tet}$  for various spinel compounds: Al (blue), Mg (red), Ca (green), Zn (orange), Li (yellow), and Na-based (brown) materials. Data are obtained and replotted from refs. [4,25].

augmenting charge carrier mobility through deliberate choices of B-group transition metals and anion chemistry that satisfy the site preference criterion. Such improvements are evident in the low migration barriers of Ca in  $d_0$ -metal oxide spinels.<sup>[4]</sup> Migration barriers in spinel materials have recently been used to derive a descriptor for the ion mobility based on ionic radii, oxidation states, and electronegativities, as mentioned in the previous section.<sup>[3]</sup> Additionally, it was shown that transport properties of spinel compounds are impacted by transition metal cations, discovering that these metals have a notable impact on the barriers for  $Mg^{2+}$  migration in such compounds.<sup>[2,87]</sup> By utilizing this principle, it was demonstrated that oxide spinels incorporating electronegative transition metal cations of substantial size hold the potential for showcasing elevated  $Mg^{2+}$  mobility.<sup>[87]</sup>

Sulfide and selenide spinels have garnered attention due to their potential as solid electrolytes in solid-state batteries. Among these compounds,  $MgSc_2Se_4$  has emerged as a promising contender with a remarkably low migration barrier of  $E_a = 0.37$  eV.<sup>[2,31–33]</sup> Nevertheless, its suitability as a solid electrolyte is impeded by a significant partial electronic conductivity. Moreover, studies have indicated that the mobility of magnesium in chalcogenide spinels that include lanthanoids escalates proportionally with the lanthanoid's size.<sup>[25,32]</sup>

## 5.2. Olivines

The utilization of an olivine structured material as positive electrode material was pioneered by the group of Goodenough in 1974.<sup>[103]</sup> This material class exhibits the general formula of  $AMXO_4$ , the A site mostly being occupied by Li, although the intercalation of other alkali metal ions has been studied as well.<sup>[104,105]</sup> The transition metal site is most popularly occupied by Fe, Mn, Co, or Ni, while X typically equals P, less often Si or Ge.<sup>[103]</sup> From a geometric point of view, the olivine structure consists of  $MO_6$  octahedra, that are connected to two  $LiO_6$  octahedra and one  $XO_4$  tetrahedra via shared edges.<sup>[106]</sup> Its crystal structure is depicted in Figure 10.

Early studies on the diffusion of charge carrier species within olivine materials assumed a strictly 1D diffusion material, con-

sisting of channels that permeate the whole crystal system in the [010] direction.<sup>[107]</sup> However, new measurements indicated a de facto 2D migration of lithium ions in the olivine structure,<sup>[108]</sup> which contradicted theoretical studies during that time that claimed the cross-channel migration to be significantly unfavored.<sup>[109]</sup> Further theoretical studies could then reveal the possibility of cross-channel diffusion, initialized by the formation of either a  $Li^+/Fe^{2+}$  antisite defect or a Frenkel defect of a  $Fe^{2+}$  ion in  $LiFePO_4$ .<sup>[110,111]</sup> This cross-channel diffusion was then found to contribute significantly to the overall migration, even at low defect concentrations.<sup>[111]</sup> Subsequently, Yang et al. could observe the cross-channel migration of lithium atoms upon the formation of antisite defects in their ab initio molecular dynamics simulations.<sup>[112]</sup> Furthermore, they determined the cross-channel diffusion to be competitive with the in-channel diffusion, finding a theoretical verification for the experimentally observed 2D migration. Therefore, while blocking diffusion in the [010]-direction, these defects open up alternative channels for the lithium ion migration.<sup>[113]</sup> Most of the published results on the diffusion coefficient for lithium ion diffusion within olivine structured materials ranges from  $10^{-11}$  to  $10^{-15}$   $cm^2 s^{-1}$ .<sup>[114]</sup> Theoretical works find energy barriers of around 0.35–0.4 eV, overestimating experimentally found diffusion coefficients.<sup>[115]</sup> These differences may be pinpointed to many factors, including the assumed uni-lateral nature of lithium ion diffusion in many theoretical works and the two phase coexistence/phase transformation during experiments.<sup>[109,116]</sup>

Olivine materials are especially interesting as energy storage materials due to their high operating potentials and high capacity, but the scientific interest in the optimization of olivine structured compounds increased even further with the recent successful commercialization of  $LiFePO_4$ .<sup>[117]</sup> Most of today's research focuses on either ridding this popular system from its known drawbacks, that is, their low energy density and slow rate performance or on the development of its derivative systems utilizing manganese, cobalt, or nickel.<sup>[118,119]</sup>

## 5.3. Garnets

The utilization of the strategy to replace  $Li^+$  ions with ions carrying greater positive charges, thereby creating vacancies through which lithium ions can migrate, has been proven effective for materials exhibiting crystal structures akin to the mineral garnet.<sup>[41,120–122]</sup>  $Ca_3Al_2Si_3O_{12}$  serves as the prototype material in this family, belonging to a group of substances known as orthosilicates, which possess isolated tetrahedral  $SiO_4$  groups. The oxide ions are arranged in layers, adopting a slightly distorted hexagonal close packing. A brief discussion on several materials sharing this structure will be presented in Section 5.8. Another example featuring a related olivine structure is the popular positive electrode material  $LiFePO_4$ , which was addressed in Section 5.2. Within the garnet structure, the  $Ca^{2+}$ ,  $Al^{3+}$ , and  $Si^{4+}$  ions exhibit 8-, 6-, and 4-fold coordination with neighboring oxide ions. It is common to find substitutions of similarly charged cations in these positions within this mineral family.

An example of a lithium-conducting solid electrolyte belonging to this group is  $Li_5La_3M_2O_{12}$ , with the M ion potentially being Nb or Ta. These materials were reported to possess lithium

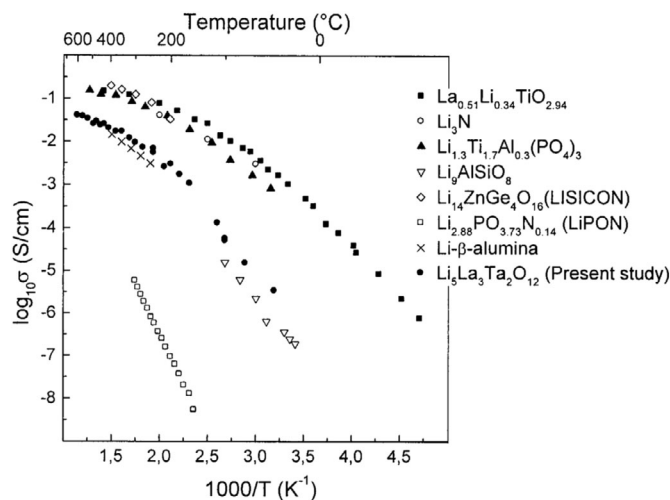


**Figure 12.** Exploring the total conductivity:  $\text{Li}_5\text{La}_3\text{Ta}_2\text{O}_{12}$  in comparison to established lithium ion conductors. Surpassing  $\text{Li}\beta$ -alumina and LiPON in conductivity, while demonstrating comparable performance to perovskite-type  $(\text{Li}, \text{La})\text{TiO}_3$  and Lisicon. Reprinted with permission.<sup>[41]</sup> The American Ceramic Society.

ion conductivities of approximately  $10^{-6} \text{ S cm}^{-1}$  at room temperature, which is roughly three orders of magnitude lower than the data reported for the previously mentioned  $(\text{La}, \text{Li})\text{TiO}_3$  materials.<sup>[123]</sup>

However, these materials can possess a significant advantage over the titanium-containing counterparts, as it has been observed that the Ta-containing version maintains its white color even when in contact with molten lithium, indicating apparent stability against highly reactive lithium. This suggests that it could be utilized in cells operating at higher output voltages compared to those limited to lower potentials.

**Figure 12** illustrates the temperature dependence of the ionic conductivity in various lithium-conducting materials.<sup>[41]</sup> The electrical conductivity activation energies for  $\text{Li}_5\text{La}_3\text{Nb}_2\text{O}_{12}$  and  $\text{Li}_5\text{La}_3\text{Ta}_2\text{O}_{12}$  at temperatures below  $300^\circ\text{C}$  are 0.43 and 0.56 eV, respectively. These values are comparable to those reported for the lithium ion conductor Lisicon (0.56 eV) and higher than the values for  $\text{Li}_3\text{N}$  (0.25 eV).  $\text{Li}_5\text{La}_3\text{Ta}_2\text{O}_{12}$  exhibits a conductivity similar to  $\text{Li}\beta$ -alumina and  $\text{Li}_9\text{AlSiO}_8$ , significantly higher than thick pellet LiPON, and slightly lower than  $\text{Li}_{14}\text{ZnGe}_4\text{O}_{16}$  and  $\text{Li}_{0.34}\text{La}_{0.51}\text{TiO}_{2.94}$ . Further investigations have also explored the replacement of some  $\text{La}^{3+}$  ions with divalent alkaline earth ions,<sup>[120]</sup> revealing that the size of the substituted ion influences the measured ionic conductivity, with the substitution of  $\text{Ba}^{2+}$  ions yielding the highest conductivity values. Although the conductivity of the modified material,  $\text{Li}_6\text{BaLa}_2\text{M}_2\text{O}_{12}$ , was slightly lower than that of the original material, it encountered fewer issues with additional grain boundary impedance. Note that the impedance measurements allow to separate single crystal from grain boundary conductivity.

Furthermore, these garnet materials exhibit stability when in contact with elemental lithium, and recent findings indicate that they do not display any reactive behavior toward several frequently employed positive electrode materials.<sup>[121]</sup>

## 5.4. Perovskites

Perovskites are crystalline phases with the general stoichiometry  $\text{ABX}_3$  where the cation on the B-site and the anion on the X-site form a rigid scaffold of corner sharing  $\text{BX}_6$  octahedra. The voids between these octahedra are occupied by the potentially mobile A-species (**Figures 10 and 13a**). The ideal perovskite structure is cubic with spacegroup  $\text{Pm}\bar{3}\text{m}$ . Most perovskites, however, attain lower symmetry due to tilted/distorted octahedra and/or displacement of the cations.

Clearly, within the battery community lithium lanthanum titanate (LLTO) is the most prominent  $\text{Li}^+$  conductor of the perovskite family. The studies of Bezou et al.<sup>[124]</sup> and Inaguma et al.<sup>[123]</sup> are commonly referred to as the first ones reporting an A-site deficient perovskite structure for  $\text{Li}_{3x}\text{La}_{2/3-x}\text{TiO}_3$  ( $0.04 < x < 0.17$ ) and bulk ionic conductivity of  $\approx 10^{-3} \text{ S cm}^{-1}$  at room temperature.<sup>[125]</sup> It has been widely acknowledged<sup>[1,125]</sup> and theoretically confirmed<sup>[126]</sup> that the diffusion proceeds via a vacancy mechanism where  $\text{Li}^+$  migrates through a bottleneck made up of four O-ions which expands in size during the diffusion process (**Figure 13b**). Evidently, the number of lattice- $\text{Li}^+$  and the number of vacancies plays a crucial role in ionic conduction, so fine tuning the parameter  $x$  has been a focus of research.<sup>[125–127]</sup> A further improvement could be achieved by widening the diffusion channel through  $\text{Sr}^{2+}$ -doping on the A-site.<sup>[128]</sup> Additionally, it has been found that depending on the synthesis route and operating temperature poorly conducting La-rich layers are formed in the crystal structure constraining the  $\text{Li}^+$  diffusion to two dimensions. This transition from the disordered to the ordered state is accompanied by a drop of one order of magnitude in conductivity.<sup>[129–132]</sup> Nevertheless, by aligning the conducting planes along the measurement direction, a value of  $4 \times 10^{-3} \text{ S cm}^{-1}$  has been recently reported for a  $13 \mu\text{m}$  single crystal.<sup>[133]</sup>

Although high resistance at the grain boundaries and low stability versus Li metal induced by  $\text{Ti}^{4+}/\text{Ti}^{3+}$  redox activity have so far prevented LLTO from application, it serves as a well-studied model system for ionic diffusion in perovskites. The replacement of  $\text{Ti}^{4+}$  with  $\text{Nb}^{5+}$ , for instance, resulting in  $\text{Li}_x\text{La}_{(1-x)/3}\text{NbO}_3$  (LLNO)<sup>[134]</sup> is an obvious idea which has gained renewed interest lately. As in the case of LLTO,  $\text{Sr}^{2+}$ -doping<sup>[135]</sup> and exploiting A-site ordering<sup>[135,136]</sup> were done to improve the material's properties; however, the bulk conductivity of  $10^{-4} \text{ S cm}^{-1}$  could hardly be increased. Exchanging the shuttle ion in LLTO from  $\text{Li}^+$  to  $\text{Na}^+$  and  $\text{Mg}^{2+}$  was not feasible owing to the very low mobility of the respective ions in the given hosts.<sup>[131,137]</sup> Nonetheless, in the case of  $\text{Na}^+$ , switching the B-site cation from  $\text{Ti}^{4+}$  to  $\text{Nb}^{5+}$  or  $\text{Zr}^{4+}$  could drastically improve the  $\text{Na}^+$  mobility exhibiting conductivity values of  $\approx 10^{-5} \text{ S cm}^{-1}$  for  $\text{Na}_{0.25}\text{La}_{0.25}\text{NbO}_3$  and  $\text{Na}_{1/3}\text{La}_{1/3}\text{Sr}_{1/3}\text{ZrO}_3$ .<sup>[138,139]</sup>

Some promising ionic conductors of an entirely different perovskite-related material's class have gained strong interest during the last decade: the so-called anti-perovskites. These compounds, usually denoted  $\text{X}_3\text{BA}$ , exhibit the typical perovskite structure while having the positions of the cations and the anions exchanged, that is, X is a cation whereas A and B are anionic species. The noteworthy breakthrough of anti-perovskites in battery research was achieved by Zhao and Daemen who reported  $\text{Li}^+$  conductivities of  $\approx 10^{-3} \text{ S cm}^{-1}$  in  $\text{Li}_3\text{OCl}_x\text{Br}_{1-x}$  ( $x = 1, 0.5$ ) at room temperature.<sup>[140]</sup> In contrary to ionic conduction in usual

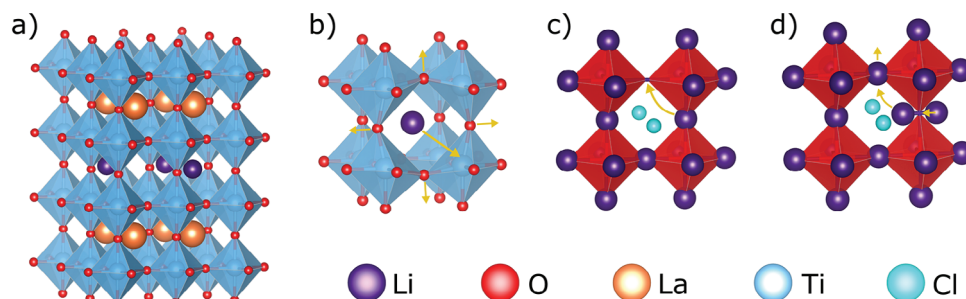


**Figure 13.** a) Lattice of ordered  $\text{Li}_{3x}\text{La}_{2/3-x}\text{TiO}_3$  perovskite exhibiting Li-rich and La-rich layers. The vacancies are located in the Li-rich layers. b) Diffusion mechanism of  $\text{Li}^+$  in  $\text{Li}_{3x}\text{La}_{2/3-x}\text{TiO}_3$  to a vacant A-site. The oxygen rectangle represents the bottleneck which expands during the diffusion process. c) Vacancy diffusion mechanism in  $\text{Li}_3\text{OCl}$  anti-perovskite along the edge of the octahedron. d) Interstitial diffusion mechanism in  $\text{Li}_3\text{OCl}$  anti-perovskite from a dumbbell configuration to a singly occupied site where a new dumbbell will be formed.

perovskites, the diffusion mechanism in  $\text{Li}_3\text{OCl}$ -type materials is an ongoing subject of discussion. Two mechanisms visualized in Figure 13c,d have been suggested: i) a vacancy mechanism where  $\text{Li}^+$  migrates along the edges of the cation octahedra to a vacant X-position; (ii) an interstitial mechanism where two  $\text{Li}^+$  are located in a X-site centered dumbbell configuration; the migration of one  $\text{Li}^+$  leaves behind a singly occupied X-site to form a new dumbbell with a neighboring  $\text{Li}^+$ .<sup>[141,142]</sup>

One recently discussed topic is the introduction of so-called superhalides (polyanions with charge -1) at the B-site of antiperovskites. Sun et al. reported the  $\text{Na}^+$  ionic conductivity of  $4.4 \times 10^{-3} \text{ S cm}^{-1}$  at room temperature in  $\text{Na}_3\text{O}(\text{BH}_4)$ , which is among the highest values measured in  $\text{Na}^+$  solid electrolytes.<sup>[143]</sup> Supported by DFT analysis, the authors attributed the outstanding conductivity to the so-called paddle-wheel mechanism, that is, the ability of the anisotropic superhalide to lower the local potential for the migrating cation by rotational motion.<sup>[143,144]</sup>

### 5.5. Prussian Blues

Prussian blue ( $\text{KFe}[\text{Fe}(\text{CN})_6]$ ) is a metal organic framework (MOF)—with the general formula  $\text{A}_{0-2}\text{M}[\text{M}'(\text{CN})_6]$  and space group  $Fm\bar{3}m$  (225)—consisting of two types of iron atoms that are octahedrally interconnected by cyanide ligands.<sup>[145]</sup> These iron atoms can be distinguished by their spin state, either high-spin ( $S=5/2$ ) or low-spin ( $S=0$ ), depending on whether they are coordinated by the nitrogen or carbon site of the cyanide ligand, respectively.<sup>[146]</sup> The possibility to exchange the M and M' sites with either electrochemically active (Mn) or inactive (Cu, Ni) transition metals adds an additional element of customizability toward the application to this material class. Furthermore, the atomic arrangement generates a spacious framework with large channels ( $\approx 1.6 \text{ \AA}$ )<sup>[147]</sup> into which a variety of cations can be intercalated into the material.<sup>[148,149]</sup>

Still, Prussian blue analogues received high scientific interest in their application as battery material only after their drastic performance improvement in 2015, when Goodenough and co-workers reported a rhombohedral modification of Prussian blue that occurred when the interstitial water was removed from a cubic, sodium-rich Prussian blue material in a drying process.<sup>[150,151]</sup> This new kind of Prussian blue indeed shows a

longer cycle life compared to the purely cubic material and a highly reversible phase transition between the modifications.<sup>[152]</sup>

The charge carriers were proposed to reside in the large body-centered voids within the Prussian blue framework since the emergence of the earliest structure model by Keggins and Miles in 1936.<sup>[145,153]</sup> Recent research on the other hand suggests that all cations independent of size try to stay in or as close to the face-centered sites as size allows and uniformly display an aversion to the body-centered void.<sup>[154,155]</sup> These suggestions are accompanied by claims that the main transport pathway throughout the cubic Prussian blue framework is not the hopping of charge carriers from body-centered void to body-centered void. Instead charge carriers prefer to move along the cyanide grid in what the authors call a ladder mechanism—always staying close to a face-centered site and revolving around an iron atom toward the next face-centered site while avoiding the body-centered voids.

The typically reported diffusion coefficients for both modifications range from  $10^{-9}$  to  $10^{-12} \text{ cm}^2 \text{ s}^{-1}$ .<sup>[156]</sup> There are a few reports that state drastically lower diffusion coefficients of  $10^{-13} \text{ cm}^2 \text{ s}^{-1}$  and below. Komayko et al. showed that for nanosized materials one does not need the assumption of a fast ionic/electronic transport in the bulk lattice, as even low apparent diffusion coefficients translate into impressive rate capabilities.<sup>[156,157]</sup> They argue that Prussian blue powders easily disperse when in contact with electrolyte and that the agglomerates are highly permeable for the electrolyte. Consequently, the shortest way of diffusion during (de-)intercalation is through the primary particles instead of diffusion through interparticle grain boundaries within the agglomerate. They suggest that one should use the size of the primary particle instead of the agglomerate size for the calculation of diffusivities, which would lower the apparent diffusion coefficients by 3–5 orders of magnitude. An overview over many experimental results can be found in the account of Komayko et al.<sup>[156]</sup> Furthermore, the diffusivities of some Prussian blue analogue structures might be limited by their effective electronic conductivity within the agglomerates, instead of slow solid state diffusion rates.<sup>[158]</sup>

Reports on theoretical calculations employed for the determination of energy barriers and diffusion coefficients in the Prussian blue framework are still scarce. Peng et al. did report energy barriers of 0.38–0.57 eV for the diffusion of sodium in nickel and cobalt Prussian blue analogue structures.<sup>[159]</sup> Their report indicates an increase in the energy barriers by about

0.1 eV when crossing the body-centered void, further verifying it as a non-equilibrium position. Furthermore, there are the reports of Nordstrand et al. utilizing a semi-empirical tight binding approach to determine the charge carrier mobility.<sup>[154,155]</sup> They report energy barriers for diffusion events from one face centered site to another to exhibit an energy barrier of 0.32–0.39 eV. The diffusion through a body-centered void is comparatively unfavored, showing energy barriers of 0.69 eV. These values closely matched the accompanying experimental diffusion coefficients, determined by cyclic voltammetry and electrochemical impedance spectroscopy measurements. The values for the energy barrier are significantly increased to 1.5 eV, when considering the diffusion through the large void created by a Fe(CN)<sub>6</sub>-vacancy. Baumgart et al. utilized first-principle calculations to calculate an activation energy of 0.3 eV for diffusion events in Prussian blue, which agree well with previous reports.<sup>[160]</sup> Furthermore, they could show that the activation energies for diffusion events in the rhombohedral and cubic modification are almost identical.

### 5.6. Chevrel Phase

The Chevrel phase (CP) is a well-known material with high ion mobility. The general formula for a Chevrel phase is Mo<sub>6</sub>T<sub>8</sub> (T=S, Se, or Te) with sulfur being the most used cage material. In its structure, a nearly cubic sulfur cage holds an octahedral molybdenum cluster forming its unique crystal structure, as depicted in Figure 10. The CP cluster structure creates cavities and channels between the blocks within the crystal lattice that are classified as 3a, 3b, and 9d according to crystallographic symmetry.<sup>[161]</sup> Sites 3a and 9d can be occupied by cations functioning as charge carriers, making them interesting candidates for potential applications in solid-state ionic conductors while sites 3b are unfavorable for cation storage due to the strong electrostatic repulsion with the face-sharing Mo atoms.<sup>[161–163]</sup> An important factor for all solid-state ionic conductors is the quick delocalization inside the material, which is directly related to cations spacing and crucial for the cation mobility. In the CP, this is achieved by the two intercalation sites at 3a and 9d. The first is the so-called inner ring site, which consists of six energetically equal sites that form a highly symmetric ring around the 3a position. The 3a position lies in a cavity which is coordinated with eight sulfur atoms, each being the corner of one CP cluster. The nearly degenerate nature of these positions, with a barrier of approximately 0.1 eV,<sup>[161]</sup> makes them favorable for accommodating a single Mg cation within the CP bulk.<sup>[5]</sup> From there, it can diffuse in all three lattice directions by passing through the channel 9d. About 0.5 Å away from the 9b site in the channel are the two outer ring sites.<sup>[164]</sup> Upon occupying all inner ring sites with one cation each, the outer ring sites can accommodate an additional Mg cation per CP cluster. The CP can take up to four electrons until its valence band is filled and the structure transforms from a metal-like material to a semiconductor, making it possible to insert up to four monovalent cations.<sup>[165]</sup> Upon intercalation of divalent Mg, the CP undergoes a two-step charge redistribution process, which is particularly fast, as X-ray photoemission spectroscopy experiments have revealed.<sup>[166]</sup> The first electron is taken up by the sulfur cage, while the second one then gets transferred to the

octahedral Mo-cluster. The CP was shown by Aurbach et al. to achieve a discharge voltage between 1 and 1.3 V, with a theoretical energy density of about 135 Wh kg<sup>-1</sup>.<sup>[167–169]</sup> From the observed plateaus in the charge/discharge curve, Aurbach et al. already inferred the existence of two different insertion sites, which could later be confirmed to be the inner and outer ring sites.

Today, it is mainly used as a cathode in magnesium batteries.<sup>[162,167,169,170]</sup> as well as for other multivalent charge carriers such as Zn<sup>2+</sup>.<sup>[171,172]</sup> It is named after the French scientist J. R. Chevrel, who first discovered it in 1973.<sup>[162,173]</sup> Using the CP as a cathode material overcomes the challenges of sluggish Mg ion insertion on the cathode side and the low reversibility of the process, which are commonly encountered issues with multivalent ions. This is attributed to the strong bonds they typically form with most cathode materials.<sup>[174]</sup> The CP's biggest advantage over other possible cathode materials is the reversibility of the insertion of charge carriers due to the minimal structural changes upon intercalation. Most other materials bind especially multivalent ions too strongly to be deintercalated during the charging process.<sup>[174]</sup> The CP, however, has a metallic ground state and thus screens the charge carrier so effectively that it can easily shield divalent charges.<sup>[165]</sup>

The sulfur cage can also be substituted with selenide and tellurium, but these elements are toxic and therefore can lead to safety problems which make them harder to handle. Many experimental studies are thus performed on the sulfur phase though research suggests that the Se phase performs with improved capacity and kinetics, even a partial substitution of Mo<sub>6</sub>S<sub>8-x</sub>Se<sub>x</sub>.<sup>[170,175,176]</sup> This is because the triclinic distortion in selenide enlarges the distance between inner sites and shortens the distance between inner and outer sites, thus opening possibilities for tailoring the ionic conductivity of the system.<sup>[177,178]</sup>

There are some theoretical reports on the diffusion of cations other than Mg, which showed a direct correlation between the ionic radius and the diffusion barrier as a descriptor for the ion mobility in the CP specifically,<sup>[5]</sup> as illustrated in **Figure 14**. This has been attributed to space limitations at the narrow transition states for migration making Pauli repulsion the main factor determining the barrier heights. There are also some studies studying the diffusion properties of Ca.<sup>[175,179]</sup> The calculations of Juran et al.<sup>[175]</sup> reach a voltage of 2.1 and 1.8 V for the respective intercalation steps of Ca using the HSE functional, which agree reasonably well with another study, which found values of 1.9 and 1.4 V for a comparable PBE functional reference calculation.<sup>[5]</sup>

There are also numerous experimental studies addressing not only the diffusion of Mg, but also other cations such as Ca,<sup>[180]</sup> Al,<sup>[181,182]</sup> Zn,<sup>[171,172,183]</sup> Na,<sup>[176]</sup> and Li.<sup>[176,184]</sup> The electronic structure and ionic diffusion properties were evaluated by phonon dispersion,<sup>[163]</sup> and in another approach, continuum modeling is employed to monitor the system. Usually the efficiency of the solid state system is limited by the reachable capacity, but was found by Drews et al. to be limited by the particle size of the Chevrel phase material with particles smaller than ≈0.5 μm being crucial to avoid transport limitations for a wide range of practical current densities.<sup>[185]</sup> Another interesting field for the CP is the usage of dual ion systems. This was investigated by Li et al., proving that the diffusion of divalent Mg ions is significantly facilitated by using a Li and Mg dual-ion system as the activation

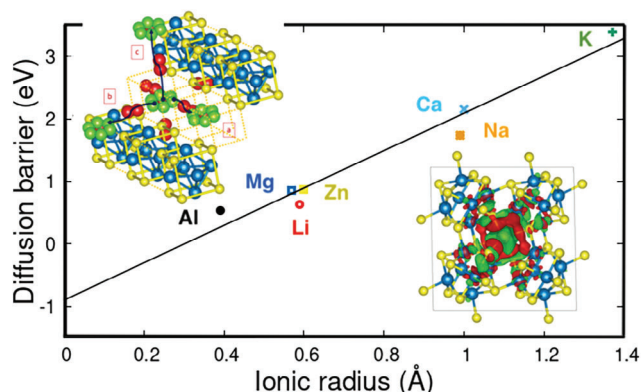


**Figure 14.** The correlation between ionic radius (in Å) and the diffusion barrier (in eV) for different charge carriers, using the revPBE+D3 functional. The ion mobility in the Chevrel phase exhibits a significant size dependence. This size dependence is evident from the linear scaling of diffusion barriers with the ion radius of the charge carriers, regardless of their charge. It suggests a distinctive and geometry-driven diffusion mechanism within the Chevrel phase. The visuals are the diffusion pathways labeled as a, b, and c on top left, connecting from the inner ring position (green) within a cavity, traverse through the outer ring positions (red), and reach the adjacent cavity with the next inner ring position, while the variation in charge density illustrated in bottom right represented regions of charge accumulation in red and areas of charge depletion in green. Reprinted with permission.<sup>[5]</sup> Published under a CC BY license.

energy is remarkably reduced specifically by the concerted interactions of preceding Li ions and following Mg ions.<sup>[186]</sup>

### 5.7. Layered Oxides

In these materials, the layers are formed by edge-sharing  $\text{MO}_6$  octahedra, in between which the alkali ions are intercalated. The stacking of the transition metal layers forms either prismatic (P) or octahedral (O) charge carrier sites with a different number of layers in the unit cell, categorized by the Delmas notation.<sup>[187]</sup> The preferred coordination environment of the charge carriers and the stacking order depend on the nature of the charge carriers and the exact stoichiometry of the material. This is apparent when comparing the stereotypical cathode materials  $\text{LiCoO}_2$  and  $\text{Na}_x\text{CoO}_2$ .  $\text{LiCoO}_2$  adopts the O3 structure,<sup>[188,189]</sup> while  $\text{Na}_x\text{CoO}_2$  can adopt either the O3, P2, or P3 structure,<sup>[190]</sup> differing in the respective oxygen stacking sequence.

In the O3 structure, diffusion can occur either via oxygen dumbbells or via tetrahedral sites when divacancy configurations are present,<sup>[191]</sup> with the divacancy mechanism exhibiting much lower barriers. In addition, the diffusion barriers were found to depend strongly on the local charge carrier configurations and thus can vary by several orders of magnitude with the charge carrier concentration.<sup>[192,193]</sup> It is noteworthy that the activation energy for the divacancy diffusion mechanism is slightly lower in  $\text{NaCoO}_2$  than in  $\text{LiCoO}_2$ <sup>[194]</sup> illustrating the non-monotonic influence of ion size on mobility. Furthermore, the presence of larger  $\text{Na}^+$  ions promotes the stability of prismatic sites, such as those found in P2 structures, and drastically influences ion mobility. As a result, complex trends of ion mobility with concentration are observed. In the P2 structure, the presence of two different prismatic Na sites ( $\text{Na}_c$  shares an edge with the  $\text{MO}_6$  octahedra,

while  $\text{Na}_f$  adopts a face-sharing coordination) destabilizes divacancy configurations, leading to a change in the diffusion mechanism in contrast to the O3 structure. While the diffusion barriers are generally lower in the P2 structure, the strong electrostatic Na-Na repulsion at high Na concentration leads to high barriers and sluggish Na diffusion.<sup>[193]</sup>

The first commercially used cathode materials for LIBs,  $\text{TiS}_2$ ,<sup>[195,196]</sup> and  $\text{LiCoO}_2$  (LCO)<sup>[197]</sup> as well as many other commercial Li cathode materials such as Ni-Mn-Co-oxide (NMC) or Ni-Co-Al oxide (NCA), crystallize in a layered structure. Layered structural motifs are also currently under intense investigation not only in the context of LIBs but also in the field of post-Lithium batteries. For example, layered oxide materials with the general formula  $\text{Na}_x\text{NO}_2$  ( $M=\text{Fe, Mn, Ni, Ti, Cr, or Co}$ ) are among the most promising cathode materials for Na-ion<sup>[198,199]</sup> and K-ion<sup>[200]</sup> batteries.

Moreover, layered structures were also shown to successfully intercalate multivalent ions such as Mg in  $\text{TiS}_2$ <sup>[201]</sup> and  $\text{TiSe}_2$ .<sup>[202]</sup> Nevertheless, the high Mg diffusion barriers of 1 eV in  $\text{TiS}_2$  require elevated temperatures to reversibly extract Mg from the structure. This strategy resulted in a high reversible capacity of  $115 \text{ mAh g}^{-1}$  at  $60^\circ\text{C}$  for  $\text{MgTiS}_2$ ,<sup>[203]</sup> however, still significant Mg entrapping in the initial cycles was found to impede the electrochemical performance. Interestingly, the mode of intercalation was found to deviate from the solid solution behavior of Li in  $\text{TiS}_2$ , and instead, Mg-vacancy orderings are found that could contribute to the observed Mg entrapping during the initial cycles.<sup>[203,204]</sup>

### 5.8. NASICON

Sodium (NA) Super Ion CONductor (NASICON) compounds were first researched as solid electrolyte material by Hong and Goodenough in 1976.<sup>[205,206]</sup> A decade later, they were adapted as positive and negative electrode materials as well.<sup>[207,208]</sup> NASICONs are polyanionic materials, which exhibit great structural stability and high ionic conductivity, especially for sodium ions. They belong to the family of superionic conductors, which are materials that display exceptionally high ionic conductivity at or near room temperature. Furthermore, they are classified as polyanionic compounds, meaning they contain anions with multiple negative charges, such as the characteristic, tetrahedral anionic units  $\text{XO}_4$  or their derivatives.<sup>[209]</sup> The NASICON structure has the general formula of  $\text{A}_x\text{MM}'(\text{XO}_4)_3$ , typical elements being  $A = \text{Li, Na, K, Mg, Ca}$ , and  $A_x = 0-5$ ,  $M/M' = \text{Fe, V, Ti, Zr, Mn}$ , and  $X = \text{S, P, Si}$ .<sup>[210]</sup> Depending on the elements used—and sometimes the content of sodium—the NASICON structure adopts many different crystal structures, the most common being rhombohedral, which consist of corner-sharing  $\text{M}/\text{M}'\text{O}_6$  octahedra and  $\text{XO}_4$  tetrahedra.<sup>[211]</sup> Within this crystal structure, there are two distinct positions for monovalent ions, often called Na1 and Na2.<sup>[212]</sup> Both are located in an  $\text{M}/\text{M}'_2(\text{XO}_4)_3$  environment—Na1 aligned along the c-axis and Na2 along the b-axis. Ions occupying the Na2 positions are the first to be extracted from the structure due to the weaker bonding caused by a longer Na-O bond lengths. The occupation of the Na2 position also leads to a significant structural rearrangement, which is inconveniently placed within the working window of batteries.<sup>[210]</sup>

Sodium ion migration in these materials is dominated by an interlayer diffusion within the [112] and [121] planes, connecting the Na1 and Na2 sites. Another migration path exists perpendicular to these planes connecting Na1 positions within different layers of sodium, which shows a much higher migration barrier. The ion mobility along the migration pathways of the NASICON structure is dominantly determined by either the formation energy of the TM redox couple or the size of the two distinct bottlenecks along the diffusion path. In the case of the bottleneck size being the determining factor, changing the elements that compose the material or introducing dopants can highly influence the migration properties.<sup>[213]</sup> Typical measured diffusion coefficients for this material are in the range of  $10^{-9}$ – $10^{-11}$  cm<sup>2</sup> s<sup>-1</sup>, with outliers of up to  $10^{-8}$  cm<sup>2</sup> s<sup>-1</sup> or down to  $10^{-15}$  cm<sup>2</sup> s<sup>-1</sup>.<sup>[210,214]</sup> Theoretically calculated values for migration barriers agree well with experimentally reported data, showing migration barriers of 0.3–0.6 eV.<sup>[210,215]</sup> Furthermore, recent studies have revealed the existence of concerted migration mechanisms for Na<sub>3</sub>Zr<sub>2</sub>Si<sub>2</sub>PO<sub>12</sub>, which can lead to significantly lower energy barrier compared to individual ion migration.<sup>[216,217]</sup>

Due to their higher charge and therefore lower occupation of crystal sites, multivalent ions like magnesium or calcium only occupy the Na1-position within the NASICON framework. The approach of utilizing multivalent charge carriers could therefore circumvent the issue of a structural change within the working window, and the halved occupation of the sodium sites leads to higher structural rigidity. Unfortunately, this also creates a longer diffusion path (no intermediate at Na2) and a more sluggish migration owed to the increased electrostatic interactions with the framework. An extensive overview over the properties of this material class can be found in the report of Alamo.<sup>[218]</sup>

## 5.9. Halide Materials

The inclusion of halide ions enhances the performance of solid electrolytes (SEs) in lithium metal batteries. Because they exhibit intrinsic high stability against oxidation (approximately 4.0 V vs. Li<sup>+</sup>/Li), as opposed to sulfide-based SEs (approximately 2.5 V), chloride-based SEs have been gaining increased attention. Given that chlorine (Cl) is more electronegative than sulfur (S), chloride-based SEs generally possess higher oxidation potentials compared to sulfide SEs. Another crucial aspect is the chemical compatibility of SEs with both the cathode active material (CAM) and metallic anodes to achieve longer lifespan, enhanced safety, and high-energy all-solid-state batteries (ASSBs). From this perspective, chloride-based SEs have demonstrated superior chemical stability with various CAMs.

In 2018, Asano and colleagues<sup>[219]</sup> conducted a revisit of the halide SSEs Li<sub>3</sub>YCl<sub>6</sub> and Li<sub>3</sub>YBr<sub>6</sub>, demonstrating impressive qualities such as high ionic conductivity at room temperature (>1 mS cm<sup>-1</sup>), excellent voltage stability, remarkable deformability, and resistance to dry air. This pioneering research has ignited significant global interest in halide SSEs.<sup>[220–226]</sup> Subsequently, a range of halide SSEs has been synthesized, encompassing various elements from fluorides to iodines. These include Li<sub>3</sub>AlF<sub>6</sub>,<sup>[227,228]</sup> Li<sub>3</sub>GaF<sub>6</sub>,<sup>[229]</sup> Li<sub>3</sub>InCl<sub>6</sub>,<sup>[220,221]</sup> Li<sub>3</sub>ScCl<sub>6</sub>,<sup>[230]</sup> spinel LiSc<sub>2/3</sub>Cl<sub>4</sub>,<sup>[231]</sup> Li<sub>3</sub>ErCl<sub>6</sub>,<sup>[232]</sup> Li<sub>3</sub>YCl<sub>6</sub>,<sup>[233,234]</sup> Li<sub>3</sub>HoCl<sub>6</sub>,<sup>[235]</sup> Li<sub>3</sub>YBr<sub>6</sub>,<sup>[236–238]</sup> Li<sub>3</sub>HoBr<sub>6</sub>,<sup>[239]</sup> Li<sub>3</sub>InBr<sub>6</sub>,<sup>[240]</sup> Li<sub>2</sub>ZrCl<sub>6</sub>,<sup>[241]</sup>

Li<sub>3</sub>LaI<sub>6</sub>,<sup>[67]</sup> and Li<sub>3</sub>ErI<sub>6</sub>.<sup>[242]</sup> Simultaneously, halide Na-ion counterparts have also emerged,<sup>[243,244]</sup> including Na<sub>2</sub>ZrCl<sub>6</sub>,<sup>[245]</sup> Na<sub>3-x</sub>Er<sub>1-x</sub>Zr<sub>x</sub>Cl<sub>6</sub>,<sup>[246]</sup> and Na<sub>3-x</sub>Y<sub>1-x</sub>Zr<sub>x</sub>Cl<sub>6</sub>.<sup>[247]</sup> In addition to these material advancements, there have been widespread reports of promising electrochemical performance based on halide SSEs, encompassing qualities such as exceptionally long cycling stability, high areal capacity, and the ability to operate at high voltages. As the search for an exceptional SSE persists, there is an essential need to comprehensively assess state-of-the-art halide SSEs, spanning from fundamental research to practical engineering applications.

## 5.10. Anion Migrations

While cation migration is well studied, less work has been done regarding the migration of anions in crystalline structures which may be used as SSEs in the growing field of halide (fluoride or chloride) ion batteries.<sup>[248–251]</sup> The most studied materials usable as SSEs in fluoride ion batteries (FIBs) are based on either rare-earth tysonite-type structures RF<sub>3</sub> (R=La, Ce, Sm) or alkaline-earth fluorite-type structures MF<sub>2</sub> (M=Ca, Ba, Sr). Ionic conductivity in tysonite-type fluorides happens by a vacancy mechanism via intrinsic Schottky defects, whereas it occurs in the fluorite-structures due to an anionic interstitial mechanism via intrinsic anti-Frenkel pairs. By homogeneous doping, the ionic conductivity can be significantly increased, as aliovalent cation substitution creates extrinsic defects, that is, anionic vacancies, in case of doped tysonite-type solid solutions R<sub>1-x</sub>M<sub>x</sub>F<sub>3-x</sub>, or interstitials, in case of doped fluorite-type solid solutions M<sub>1-x</sub>R<sub>x</sub>F<sub>2+x</sub>.<sup>[252]</sup> The first rechargeable FIB employed the nanocrystalline Ba-doped tysonite La<sub>0.9</sub>Ba<sub>0.1</sub>F<sub>2.9</sub> as SSE with a fluoride ion conductivity of  $2.8 \times 10^{-4}$  S cm<sup>-1</sup> at 160 °C.<sup>[253]</sup> By employing single crystals of La<sub>0.9</sub>Ba<sub>0.1</sub>F<sub>2.9</sub>, a comparable ion conductivity can already be achieved at room temperature. Yet, as single crystals are difficult to implement into batteries, attempts to improve the ionic conductivity of polycrystalline materials have been made. In detailed studies on the ion conduction mechanism in FIBs, Rongeat et al. revealed, that grain boundaries lead to noticeable blocking effects in tysonite-type fluorides and that heat treatment of the polycrystalline tysonite-type SSE can significantly enhance the ionic conductivity.<sup>[254]</sup> In contrast, due to the different ion conduction mechanisms in fluorite-type materials, the ionic conductivity of the La-doped fluorite Ba<sub>1-x</sub>La<sub>x</sub>F<sub>2+x</sub> can be improved by increasing the number of grain boundaries via nanostructuring, as it offers additional conduction paths for the motion of vacancies along the grain boundaries, yielding an optimum ionic conductivity for Ba<sub>0.6</sub>La<sub>0.4</sub>F<sub>2.4</sub> of  $1.9 \times 10^{-4}$  S cm<sup>-1</sup> at 160 °C.<sup>[255]</sup> Yet, for the polycrystalline fluorite- or tysonite-type compounds discussed so far, sufficient ion conductivity can only be achieved at temperatures above 150 °C. Only in the form of sintered disks, which cannot be integrated into batteries, Sm<sub>0.95</sub>Ca<sub>0.05</sub>F<sub>2.95</sub> and Ce<sub>0.975</sub>Sr<sub>0.025</sub>F<sub>2.975</sub> yield conductivities of  $1 \times 10^{-4}$  or  $3 \times 10^{-4}$  S cm<sup>-1</sup> at room temperature.<sup>[256,257]</sup> Still, Dieudonné et al. employed these systematic studies with Ca- and Sr-doped tysonite-type SmF<sub>3</sub> or CeF<sub>3</sub> structures<sup>[256,257]</sup> to reveal valuable structure-property-relations: They found that the difference between the ionic radii of M<sup>2+</sup> and R<sup>3+</sup> plays a key role for structural features such as buckling effects which in turn have a strong impact on the fluoride con-

ductivity. As outlined earlier, such a relationship can assist the search for new ionic conductors.

Besides, ternary systems, such as the Sn-based metal fluorides  $\text{MSnF}_4$  ( $M=\text{Pb, Ba, Sr}$ ), show a very high ionic conductivity ( $10^{-3}$  to  $10^{-4}$   $\text{S cm}^{-1}$ ) at room temperature.<sup>[258]</sup> The superionic conductivity has been related to the disorder caused by the stereo-activity of  $\text{Sn}^{2+}$  lone pairs.<sup>[259]</sup> Repulsive interactions between the electron lone pair and F ions occur, leading to a depletion of F ions in the  $\text{Sn}^{2+}$  containing layers of the crystal and an increase in the fluoride ion mobility within these layers.<sup>[250]</sup> Mohammad et al. proved that  $\text{BaSnF}_4$  can be used as a solid electrolyte in room temperature FIBs.<sup>[260]</sup>

Finally, the corner-sharing network of the octahedral building blocks in halide perovskites  $\text{ABX}_3$  can also allow facile, vacancy-mediated anion migration.<sup>[261]</sup> By employing a K-doped  $\text{CsPbF}_3$  perovskite ( $\text{CsPb}_{0.9}\text{K}_{0.1}\text{F}_{2.9}$ ), an ionic conductivity of  $1.23 \times 10^{-3}$   $\text{S cm}^{-1}$  at room temperature could be achieved by Wang et al.<sup>[262]</sup> Moreover, this fluoride conducting SSE exhibits an ESW, which is significantly wider than that of  $\text{BaSnF}_4$  or  $\text{PbSnF}_4$ .<sup>[262]</sup> Such a desired combination of a high ionic conductivity at room temperature and a high electrochemical stability has also been found for the chloride perovskite  $\text{CsSnCl}_3$  ( $\sigma = 3.6 \times 10^{-4}$   $\text{S cm}^{-1}$ , width of ESW: 6.1 V), which can be used as SSE for chloride ion batteries. In this study, the creation of a high amount of nanograins, lattice strain, and tin vacancies during synthesis assured the structural stability of the cubic  $\text{CsSnCl}_3$  phase against the transition to its monoclinic phase.<sup>[263]</sup>

Trends in the migration barriers within different halide perovskites have been explained by the trends in the B-X covalency: the stronger the covalent character, the higher the ion migration barrier.<sup>[261,264]</sup> Covalency has been determined either by the relative energetic positions of the band center of the B-site cation and the isolated halogen atom<sup>[261]</sup> or based on the crystal orbital Hamiltonian population.<sup>[264]</sup> These or similar descriptors might be useful for the development of further SSEs in halide ion batteries.

## 6. Conclusion and Perspective

This review emphasizes the ion mobility in crystalline battery materials, encompassing both electrolytes and electrodes, and reveals a crucial distinction between their roles. Electrolytes act as ion conductors while maintaining the role of an electronic insulator to prevent the uncontrolled flow of electrons during battery operation. On the other hand, electrodes must serve as both ion and electron conductors to facilitate the recombination of ions and electrons upon their entry into the electrodes. Despite these divergent functions, from a quantum chemical perspective, the determination of migration properties depends on the minimum energy path connecting two equivalent intercalation sites and the maximum activation barrier along this path. This insight highlights the essential similarity in the migration behavior of ions in both electrolytes and electrodes, emphasizing the importance of understanding and optimizing ion mobility for the development of advanced and efficient battery materials.

We explored the potential for establishing descriptors for ionic conductivities that can universally correlate across different structural families. Such descriptors could greatly accelerate the discovery of new ion conductors with superionic conductivity.

High ionic conductivity has been correlated with electrodes and electrolytes featuring body-centered cubic anion sublattices and structures where the mobile species is not in its preferred coordination. Besides these structural considerations, the connection between ionic size, oxidation state, and electronegativity of compound species can describe ionic conductivity for various cation and anion chemistries in different structural families. Furthermore, within the spinel structure, the migration barrier of mobile cations demonstrates a volcano-like trend, where the optimal activation energies are achieved when the site preference between two inequivalent minima tends toward zero. These correlations suggest a promising path for identifying new superionic conductors. Moreover, enhancing ionic conductivities among different types of materials including silver, sodium, lithium, and fluorine ions, has been demonstrated by lowering the frequency of low-energy optical phonons. These hypotheses, however, require further experimental and computational investigation.

Little attention has been paid so far to limitations of the ion mobility due to structural constraints at the interface between the solid electrolyte and electrode. The interaction between SSEs and electrode materials can limit the practical use in batteries as it may lead to interfacial structures that impede the transfer of ions. The reasons for this behavior are not well understood yet. Future research is necessary to comprehend the reaction mechanisms at the interface between fast ion conductors and conventional electrode materials, as well as between different fast ion conductors. The goal is to develop solutions that stabilize these interfaces. Understanding and controlling interfacial reactivity is crucial for leveraging space charge layers created in multicomponent ion conductors for enhanced ion conductivity through nanostructural designs. It is also important to minimize interface reactivity by protecting ion conductors with surface coatings.

## Acknowledgements

Financial support by the German Research Foundation (DFG) through Project ID 390 874 152 (EXC 2154, POLIS Cluster of Excellence) and by the Dr. Barbara Mez-Starck Foundation is gratefully acknowledged. The authors furthermore acknowledge computer time provided by the state of Baden-Württemberg through the bwHPC program and the German Research Foundation (DFG) through Grant no. INST 40/575-1 FUGG (JUSTUS 2 cluster). This work contributes to the research performed at CELEST (Center for Electrochemical Energy Storage Ulm-Karlsruhe).

Open access funding enabled and organized by Projekt DEAL.

## Conflict of Interest

The authors declare no conflict of interest.

## Keywords

density functional theory, electrodes, ion mobility, migration barriers, solid electrolytes

Received: August 4, 2023

Revised: October 22, 2023

Published online:

- [1] J. C. Bachman, S. Muy, A. Grimaud, H.-H. Chang, N. Pour, S. F. Lux, O. Paschos, F. Maglia, S. Lupart, P. Lamp, L. Giordano, Y. Shao-Horn, *Chem. Rev.* **2016**, *116*, 140.
- [2] M. Sotoudeh, M. Dillenz, A. Groß, *Adv. Energy Sustainability Res.* **2021**, *2*, 2100113.
- [3] M. Sotoudeh, A. Groß, *JACS Au* **2022**, *2*, 463.
- [4] M. Dillenz, M. Sotoudeh, C. Glaser, J. Janek, A. Groß, H. Euchner, *Batter. Supercaps* **2022**, *5*, e202200164.
- [5] K. Helmbrecht, H. Euchner, A. Groß, *Batter. Supercaps* **2022**, *5*, e202200002.
- [6] T. Famprikis, P. Canepa, J. A. Dawson, M. S. Islam, C. Masquelier, *Nat. Mater.* **2019**, *18*, 1278.
- [7] C. A. Wert, *Phys. Rev.* **1950**, *79*, 601.
- [8] G. H. Vineyard, *J. Phys. Chem. Sol.* **1957**, *3*, 121.
- [9] P. Hänggi, P. Talkner, M. Borkovec, *Rev. Mod. Phys.* **1990**, *62*, 251.
- [10] A. Marcolongo, N. Marzari, *Phys. Rev. Mater.* **2017**, *1*, 025402.
- [11] Z. Li, R. P. Misra, Y. Li, Y.-C. Yao, S. Zhao, Y. Zhang, Y. Chen, D. Blankschtein, A. Noy, *Nat. Nanotechnol.* **2023**, *18*, 177.
- [12] J. Frenkel, *Z. Physik* **1926**, *35*, 652.
- [13] C. Wagner, W. Schottky, *Z. Phys. Chem. B* **1930**, *11*, 163.
- [14] H. Mehrer, *Diffusion in Solids: Fundamentals, Methods, Materials, Diffusion-Controlled Processes*, Springer Series in Solid-State Sciences, Springer Berlin Heidelberg, **2007**.
- [15] D. Mahlberg, A. Groß, *ChemPhysChem* **2021**, *22*, 29.
- [16] C. Tubandt, E. Lorenz, *Z. Phys. Chem.* **1914**, *87U*, 513.
- [17] R. J. Friauf, *Phys. Rev.* **1957**, *105*, 843.
- [18] R. J. Friauf, *J. Appl. Phys.* **2004**, *33*, 494.
- [19] A. Groß, S. Sakong, *Curr. Opin. Electrochem.* **2019**, *14*, 1.
- [20] J. B. Grinderslev, L. N. Skov, J. G. Andreasen, S. Ghorwal, J. Skibsted, T. R. Jensen, *Angew. Chem. Int. Ed.* **2022**, *61*, e202203484.
- [21] Y. Yan, W. Dononelli, M. Jørgensen, J. B. Grinderslev, Y.-S. Lee, Y. W. Cho, R. Černý, B. Hammer, T. R. Jensen, *Phys. Chem. Chem. Phys.* **2020**, *22*, 9204.
- [22] J. Janek, W. G. Zeier, *Nat. Energy* **2023**, *8*, 230.
- [23] T. Chen, G. Ceder, G. Sai Gautam, P. Canepa, *Front. Chem.* **2019**, *7*, 24.
- [24] T. Chen, G. Sai Gautam, P. Canepa, *Chem. Mater.* **2019**, *31*, 8087.
- [25] M. Sotoudeh, A. Groß, *J. Phys. Chem. Lett.* **2022**, *13*, 10092.
- [26] S. Ikeda, M. Takahashi, J. Ishikawa, K. Ito, *Solid State Ion.* **1987**, *23*, 125.
- [27] Z. Halim, S. Adnan, N. Mohamed, *Ceram. Int.* **2016**, *42*, 4452.
- [28] R. Mohtadi, M. Matsui, T. S. Arthur, S.-J. Hwang, *Angew. Chem. Int. Ed.* **2012**, *51*, 9780.
- [29] A. Unemoto, M. Matsuo, S.-i. Orimo, *Adv. Funct. Mater.* **2014**, *24*, 2267.
- [30] S. Higashi, K. Miwa, M. Aoki, K. Takechi, *Chem. Commun.* **2014**, *50*, 1320.
- [31] P. Canepa, S.-H. Bo, G. Sai Gautam, B. Key, W. D. Richards, T. Shi, Y. Tian, Y. Wang, J. Li, G. Ceder, *Nat. Commun.* **2017**, *8*, 1759.
- [32] J. Koettgen, C. J. Bartel, G. Ceder, *Chem. Commun.* **2020**, *56*, 1952.
- [33] M. Dillenz, M. Sotoudeh, H. Euchner, A. Groß, *Front. Energy Res.* **2020**, *8*, 260.
- [34] M. Liu, Z. Rong, R. Malik, P. Canepa, A. Jain, G. Ceder, K. A. Persson, *Energy Environ. Sci.* **2015**, *8*, 964.
- [35] Q. Zhao, L. Pan, Y.-J. Li, L.-Q. Chen, S.-Q. Shi, *Rare Met.* **2018**, *37*, 497.
- [36] A. Manthiram, X. Yu, S. Wang, *Nat. Rev. Mater.* **2017**, *2*, 16103.
- [37] F. C. Frank, D. Turnbull, *Phys. Rev.* **1956**, *104*, 617.
- [38] U. Gösele, W. Frank, A. Seeger, *Appl. Phys.* **1980**, *23*, 361.
- [39] T. Y. Tan, U. Gösele, in *Diffusion in Condensed Matter: Methods, Materials, Models*, (Eds: P. Heitjans, J. Kärger), Springer Berlin Heidelberg, Berlin, Heidelberg **2005**, pp. 165–208.
- [40] S. Sakong, C. Mosch, A. Lozano, H. F. Busnengo, A. Groß, *ChemPhysChem* **2012**, *13*, 3467.
- [41] V. Thangadurai, H. Kaack, W. J. F. Weppner, *J. Am. Ceram. Soc.* **2003**, *86*, 437.
- [42] J. Allen, J. Wolfenstine, E. Rangasamy, J. Sakamoto, *J. Power Sources* **2012**, *206*, 315.
- [43] X. He, Y. Zhu, Y. Mo, *Nat. Commun.* **2017**, *8*, 15893.
- [44] B. Doliwa, A. Heuer, *Phys. Rev. E* **2000**, *61*, 6898.
- [45] B. Kozinsky, in *Handbook of Materials Modeling: Applications: Current and Emerging Materials*, (Eds: W. Andreoni, S. Yip), Springer International Publishing, Cham **2018**, pp. 1–20.
- [46] R. Jalem, Y. Yamamoto, H. Shiiba, M. Nakayama, H. Munakata, T. Kasuga, K. Kanamura, *Chem. Mater.* **2013**, *25*, 425.
- [47] L. Zhou, N. Minafra, W. G. Zeier, L. F. Nazar, *Acc. Chem. Res.* **2021**, *54*, 2717.
- [48] W. D. Richards, T. Tsujimura, L. J. Miara, Y. Wang, J. C. Kim, S. P. Ong, I. Uechi, N. Suzuki, G. Ceder, *Nat. Commun.* **2016**, *7*, 11009.
- [49] L. Zhou, A. Assoud, Q. Zhang, X. Wu, L. F. Nazar, *J. Am. Chem. Soc.* **2019**, *141*, 19002.
- [50] Y. Chen, C. J. Bartel, M. Avdeev, Y.-Q. Zhang, J. Liu, P. Zhong, G. Zeng, Z. Cai, H. Kim, H. Ji, G. Ceder, *Chem. Mater.* **2021**, *34*, 128.
- [51] G. Frenking, A. Krapp, *J. Comput. Chem.* **2007**, *28*, 15.
- [52] M. Cho, N. Sylvetsky, S. Eshafi, G. Santra, I. Efremenko, J. M. L. Martin, *ChemPhysChem* **2020**, *21*, 688.
- [53] J. Zhao, Z.-W. Zhu, D.-X. Zhao, Z.-Z. Yang, *Phys. Chem. Chem. Phys.* **2023**, *25*, 9020.
- [54] W. H. Eugen Schwarz, F. Richard, *Ber. Bunsenges. Phys. Chem.* **1991**, *95*, 1308.
- [55] J. Béjar, L. Álvarez-Contreras, F. Espinosa-Magaña, J. Ledesma-García, N. Arjona, L. G. Arriaga, *Electrochim. Acta* **2021**, *391*, 138900.
- [56] B. J. Kwon, L. Yin, H. Park, P. Parajuli, K. Kumar, S. Kim, M. Yang, M. Murphy, P. Zapol, C. Liao, T. T. Fister, R. F. Klie, J. Cabana, J. T. Vaughey, S. H. Lapidus, B. Key, *Chem. Mater.* **2020**, *32*, 6577.
- [57] L. Li, Y.-M. Gan, Z.-H. Lu, X. Yu, S. Qing, Z. Gao, R. Zhang, G. Feng, *Appl. Surf. Sci.* **2020**, *521*, 146478.
- [58] F. Zasada, P. V. B. Pinho, W. Piskorz, C. Hudy, J. Janas, J. Gryboś, K. Góra-Marek, Z. Sojka, *J. Phys. Chem. C* **2020**, *124*, 19681.
- [59] Y. Cao, J. Liang, X. Li, L. Yue, Q. Liu, S. Lu, A. M. Asiri, J. Hu, Y. Luo, X. Sun, *Chem. Commun.* **2021**, *57*, 2343.
- [60] C. Zhao, Z. Yao, Q. Wang, H. Li, J. Wang, M. Liu, S. Ganapathy, Y. Lu, J. Cabana, B. Li, X. Bai, A. Aspuru-Guzik, M. Wagemaker, L. Chen, Y.-S. Hu, *J. Am. Chem. Soc.* **2020**, *142*, 5742.
- [61] A. Pramanik, A. G. Manche, R. Clulow, P. Lightfoot, A. R. Armstrong, *Dalton Trans.* **2022**, *51*, 12467.
- [62] X. He, H. Sun, X. Ding, K. Zhao, *J. Phys. Chem. C* **2021**, *125*, 10284.
- [63] R. S. Mulliken, *J. Chem. Phys.* **2004**, *23*, 1833.
- [64] M. Hammouri, M. Arsentev, A. Petrov, *Mater. Today Commun.* **2019**, *20*, 100598.
- [65] F.-D. Yu, L.-F. Que, C.-Y. Xu, M.-J. Wang, G. Sun, J.-G. Duh, Z.-B. Wang, *Nano Energy* **2019**, *59*, 527.
- [66] F. Heidar-Zadeh, P. W. Ayers, T. Verstraelen, I. Vinogradov, E. Vöhringer-Martinez, P. Bultinck, *J. Phys. Chem. A* **2018**, *122*, 4219.
- [67] Z. Xu, X. Chen, K. Liu, R. Chen, X. Zeng, H. Zhu, *Chem. Mater.* **2019**, *31*, 7425.
- [68] C. Fonseca Guerra, J.-W. Handgraaf, E. J. Baerends, F. M. Bickelhaupt, *J. Comp. Chem.* **2004**, *25*, 189.
- [69] S. A. Sozykin, V. P. Beskachko, *Fuller. Nanotub.* **2022**, *30*, 199.
- [70] S. Ullah, P. A. Denis, F. Sato, *Int. J. Quantum Chem.* **2019**, *119*, e25975.
- [71] B. Wang, S. L. Li, D. G. Truhlar, *J. Chem. Theory Comput.* **2014**, *10*, 5640.
- [72] B. Han, C. M. Isborn, L. Shi, *J. Chem. Theory Comput.* **2021**, *17*, 889.
- [73] C. Ertural, R. P. Stoffel, P. C. Müller, C. A. Vogt, R. Dronskowski, *Chem. Mater.* **2022**, *34*, 652.
- [74] S. Posysaev, O. Miroshnichenko, M. Alatalo, D. Le, T. S. Rahman, *Comput. Mater. Sci.* **2019**, *161*, 403.



- [75] M. Scheffler, M. Aeschlimann, M. Albrecht, T. Bereau, H.-J. Bungartz, C. Felser, M. Greiner, A. Groß, C. T. Koch, K. Kremer, W. E. Nagel, M. Scheidgen, C. Wöll, C. Draxl, *Nature* **2022**, 604, 635.
- [76] L. M. Ghiringhelli, J. Vybiral, S. V. Levchenko, C. Draxl, M. Scheffler, *Phys. Rev. Lett.* **2015**, 114, 105503.
- [77] O. Isayev, C. Oses, C. Toher, E. Gossett, S. Curtarolo, A. Tropsha, *Nat. Commun.* **2017**, 8, 15679.
- [78] J. K. Nørskov, J. Rossmeisl, A. Logadottir, L. Lindqvist, J. R. Kitchin, T. Bligaard, H. Jónsson, *J. Phys. Chem. B* **2004**, 108, 17886.
- [79] I. C. Man, H.-Y. Su, F. Calle-Vallejo, H. A. Hansen, J. I. Martinez, N. G. Inoglu, J. Kitchin, T. F. Jaramillo, J. K. Nørskov, J. Rossmeisl, *ChemCatChem* **2011**, 3, 1159.
- [80] M. Jäckle, K. Helmbrecht, M. Smits, D. Stottmeister, A. Groß, *Energy Environ. Sci.* **2018**, 11, 3400.
- [81] Y. Wang, W. D. Richards, S. P. Ong, L. J. Miara, J. C. Kim, Y. Mo, G. Ceder, *Nat. Mater.* **2015**, 14, 1026.
- [82] S. Muy, J. C. Bachman, L. Giordano, H.-H. Chang, D. L. Abernathy, D. Bansal, O. Delaire, S. Hori, R. Kanno, F. Maglia, S. Lupart, P. Lamp, Y. Shao-Horn, *Energy Environ. Sci.* **2018**, 11, 850.
- [83] K. Gordiz, S. Muy, W. G. Zeier, Y. Shao-Horn, A. Henry, *Cell Rep.* **2021**, 2, 100431.
- [84] Z. Rong, R. Malik, P. Canepa, G. Sai Gautam, M. Liu, A. Jain, K. Persson, G. Ceder, *Chem. Mater.* **2015**, 27, 6016.
- [85] K. Wakamura, *Phys. Rev. B* **1997**, 56, 11593.
- [86] U. Köhler, C. Herzog, *Philos. Mag. A* **1988**, 58, 769.
- [87] M. Sotoudeh, M. Dillenz, J. Döhn, J. Hansen, S. Dsoke, A. Groß, *Chem. Mater.* **2023**, 35, 4786.
- [88] K. Kim, D. J. Siegel, *J. Mater. Chem. A* **2022**, 10, 15169.
- [89] R. Jalem, M. Nakayama, T. Kasuga, *J. Mater. Chem. A* **2014**, 2, 720.
- [90] R. Jalem, M. Kimura, M. Nakayama, T. Kasuga, *J. Chem. Inf. Model.* **2015**, 55, 1158.
- [91] N. Kireeva, V. S. Pervov, *Phys. Chem. Chem. Phys.* **2017**, 19, 20904.
- [92] A. D. Sendek, Q. Yang, E. D. Cubuk, K.-A. N. Duerloo, Y. Cui, E. J. Reed, *Energy Environ. Sci.* **2017**, 10, 306.
- [93] L. Zhang, B. He, Q. Zhao, Z. Zou, S. Chi, P. Mi, A. Ye, Y. Li, D. Wang, M. Avdeev, S. Adams, S. Shi, *Adv. Funct. Mater.* **2020**, 30, 2003087.
- [94] C. Ling, F. Mizuno, *Chem. Mater.* **2013**, 25, 3062.
- [95] H. Euchner, O. Clemens, M. A. Reddy, *Npj Comput. Mater.* **2019**, 5, 31.
- [96] A. Rutt, D. Sari, Q. Chen, J. Kim, G. Ceder, K. A. Persson, *ACS Appl. Mater. Interfaces* **2023**, 15, 34983.
- [97] S.-H. Yang, H. Xue, S.-P. Guo, *Coord. Chem. Rev.* **2021**, 427, 213551.
- [98] N. Zhang, Y. Dong, M. Jia, X. Bian, Y. Wang, M. Qiu, J. Xu, Y. Liu, L. Jiao, F. Cheng, *ACS Energy Lett.* **2018**, 3, 1366.
- [99] L. Campanella, G. Pistoia, *J. Electrochem. Soc.* **1971**, 118, 1905.
- [100] H. Lahan, S. K. Das, *J. Power Sources* **2019**, 413, 134.
- [101] R. D. Bayliss, B. Key, G. Sai Gautam, P. Canepa, B. J. Kwon, S. H. Lapidus, F. Dogan, A. A. Adil, A. S. Lipton, P. J. Baker, G. Ceder, J. T. Vaughey, J. Cabana, *Chem. Mater.* **2020**, 32, 663.
- [102] T. Chen, G. Sai Gautam, W. Huang, G. Ceder, *Chem. Mater.* **2018**, 30, 153.
- [103] A. K. Padhi, K. S. Nanjundaswamy, J. B. Goodenough, *J. Electrochem. Soc.* **1997**, 144, 1188.
- [104] Y. Wang, R. Chen, T. Chen, H. Lv, G. Zhu, L. Ma, C. Wang, Z. Jin, J. Liu, *Energy Storage Mater.* **2016**, 4, 103.
- [105] K. T. Lee, T. Ramesh, F. Nan, G. Botton, L. F. Nazar, *Chem. Mater.* **2011**, 23, 3593.
- [106] M. H. Alfaruqi, S. Kim, S. Park, S. Lee, J. Lee, J.-Y. Hwang, Y.-K. Sun, J. Kim, *ACS Appl. Mater. Interfaces* **2020**, 12, 16376.
- [107] N. Tolganbek, Y. Yerkinbekova, S. Kalybekkyzy, Z. Bakenov, A. Mentbayeva, *J. Alloys Compd.* **2021**, 882, 160774.
- [108] R. Amin, J. Maier, P. Balaya, D. Chen, C. Lin, *Solid State Ion.* **2008**, 179, 1683.
- [109] D. Morgan, A. Van der Ven, G. Ceder, *Electrochem. Solid-State Lett.* **2003**, 7, A30.
- [110] S. Adams, *J. Solid State Electrochem.* **2010**, 14, 1787.
- [111] R. Malik, D. Burch, M. Bazant, G. Ceder, *Nano Lett.* **2010**, 10, 4123.
- [112] J. Yang, J. S. Tse, *J. Phys. Chem. A* **2011**, 115, 13045.
- [113] C. Delacourt, L. Laffont, R. Bouchet, C. Wurm, J.-B. Leriche, M. Morcrette, J.-M. Tarascon, C. Masquelier, *J. Electrochem. Soc.* **2005**, 152, A913.
- [114] H. Yang, C. Fu, Y. Sun, L. Wang, T. Liu, *Carbon* **2020**, 158, 102.
- [115] S. Kanungo, A. Bhattacharjee, N. Bahadursha, A. Ghosh, *Nanomaterials* **2022**, 12, 3266.
- [116] T. Flack, S. A. Jobbins, S. E. Boulfelfel, S. Leoni, *J. Phys. Chem. C* **2022**, 126, 12339.
- [117] D. Anseán, M. Dubarry, A. Devie, B. Liaw, V. García, J. Viera, M. González, *J. Power Sources* **2017**, 356, 36.
- [118] A. Mauger, C. M. Julien, *Batteries* **2018**, 4, 39.
- [119] L. Yang, W. Deng, W. Xu, Y. Tian, A. Wang, B. Wang, G. Zou, H. Hou, W. Deng, X. Ji, *J. Mater. Chem. A* **2021**, 9, 14214.
- [120] V. Thangadurai, W. Weppner, *J. Am. Ceram. Soc.* **2005**, 88, 411.
- [121] V. Thangadurai, W. Weppner, *J. Power Sources* **2005**, 142, 339.
- [122] R. Murugan, V. Thangadurai, W. Weppner, *J. Electrochem. Soc.* **2007**, 155, A90.
- [123] Y. Inaguma, C. Liqun, M. Itoh, T. Nakamura, T. Uchida, H. Ikuta, M. Wakihara, *Solid State Commun.* **1993**, 86, 689.
- [124] A. Belous, G. Novitskaya, S. Polyanetskaya, Y. I. Gornikov, *Izv. Akad. Nauk SSSR, Neorg. Mater* **1987**, 23, 470.
- [125] S. Stramare, V. Thangadurai, W. Weppner, *Chem. Mater.* **2003**, 15, 3974.
- [126] C.-h. Chen, J. Du, *J. Am. Ceram. Soc.* **2015**, 98, 534.
- [127] J. Ibarra, A. Várez, C. León, J. Santamaria, L. Torres-Martinez, J. Sanz, *Solid State Ion.* **2000**, 134, 219.
- [128] Y. Inaguma, L. Chen, M. Itoh, T. Nakamura, *Solid State Ion.* **1994**, 70, 196.
- [129] Y. Harada, Y. Hirakoso, H. Kawai, J. Kuwano, *Solid State Ion.* **1999**, 121, 245.
- [130] E. Jay, M. Rushton, A. Chronos, R. Grimes, J. Kilner, *Phys. Chem. Chem. Phys.* **2015**, 17, 178.
- [131] A. R. Symington, J. Purton, J. Statham, M. Molinari, M. S. Islam, S. C. Parker, *J. Mater. Chem. A* **2020**, 8, 19603.
- [132] G. Hasegawa, N. Kuwata, K. Hashi, Y. Tanaka, K. Takada, *Chem. Mater.* **2023**, 35, 3815.
- [133] S. Kobayashi, D. Yokoe, Y. Fujiwara, K. Kawahara, Y. Ikuhara, A. Kuwabara, *Nano Lett.* **2022**, 22, 5516.
- [134] A. Belous, E. Pashkova, O. Gavrilenko, O. V'yunov, L. Kovalenko, *J. Eur. Ceram. Soc.* **2004**, 24, 1301.
- [135] Z. Yang, S. Suzuki, N. Tanibata, H. Takeda, M. Nakayama, M. Karasuyama, I. Takeuchi, *J. Phys. Chem. C* **2020**, 125, 152.
- [136] J. Hong, S. Kobayashi, A. Kuwabara, Y. H. Ikuhara, Y. Fujiwara, Y. Ikuhara, *Molecules* **2021**, 26, 3559.
- [137] C. Pérez-Vicente, A. Medina, R. Alcantara, *ACS Appl. Energy Mater.* **2022**, 5, 15749.
- [138] Y. Kong, Y. Liu, G. Hu, *Ceram. Int.* **2022**, 48, 36136.
- [139] Y. Zhao, Z. Liu, J. Xu, T. Zhang, F. Zhang, X. Zhang, *J. Alloys Compd.* **2019**, 783, 219.
- [140] Y. Zhao, L. L. Daemen, *J. Am. Chem. Soc.* **2012**, 134, 15042.
- [141] J. A. Dawson, T. Famprikis, K. E. Johnston, *J. Mater. Chem. A* **2021**, 9, 18746.
- [142] W. Xia, Y. Zhao, F. Zhao, K. Adair, R. Zhao, S. Li, R. Zou, Y. Zhao, X. Sun, *Chem. Rev.* **2022**, 122, 3763.
- [143] Y. Sun, Y. Wang, X. Liang, Y. Xia, L. Peng, H. Jia, H. Li, L. Bai, J. Feng, H. Jiang, J. Xie, *J. Am. Chem. Soc.* **2019**, 141, 5640.
- [144] Z. Zhang, L. F. Nazar, *Nat. Rev. Mater.* **2022**, 7, 389.
- [145] J. Keggins, F. Miles, *Nature* **1936**, 137, 577.

- [146] F. S. Hegner, J. R. Galán-Mascarós, N. López, *Inorg. Chem.* **2016**, *55*, 12851.
- [147] K. Itaya, I. Uchida, V. D. Neff, *Acc. Chem. Res.* **1986**, *19*, 162.
- [148] K. Itaya, T. Ataka, S. Toshima, *J. Am. Chem. Soc.* **1982**, *104*, 4767.
- [149] A. Kraft, *Ionics* **2021**, *27*, 2289.
- [150] L. Wang, J. Song, R. Qiao, L. A. Wray, M. A. Hossain, Y.-D. Chuang, W. Yang, Y. Lu, D. Evans, J.-J. Lee, S. Vail, X. Zhao, M. Nishijima, S. Kakimoto, J. B. Goodenough, *J. Am. Chem. Soc.* **2015**, *137*, 2548.
- [151] J. Song, L. Wang, Y. Lu, J. Liu, B. Guo, P. Xiao, J.-J. Lee, X.-Q. Yang, G. Henkelman, J. B. Goodenough, *J. Am. Chem. Soc.* **2015**, *137*, 2658.
- [152] W. Wang, Y. Gang, Z. Hu, Z. Yan, W. Li, Y. Li, Q.-F. Gu, Z. Wang, S.-L. Chou, H.-K. Liu, S.-X. Dou, *Nat. Commun.* **2020**, *11*, 980.
- [153] F. Herren, P. Fischer, A. Ludi, W. Hälg, *Inorg. Chem.* **1980**, *19*, 956.
- [154] J. Nordstrand, E. Toledo-Carrillo, S. Vafakhah, L. Guo, H. Y. Yang, L. Kloo, J. Dutta, *ACS Appl. Mater. Interfaces* **2021**, *14*, 1102.
- [155] J. Nordstrand, E. Toledo-Carrillo, L. Kloo, J. Dutta, *Phys. Chem. Chem. Phys.* **2022**, *24*, 12374.
- [156] A. I. Komayko, N. A. Arkharova, D. E. Presnov, E. E. Levin, V. A. Nikitina, *J. Phys. Chem.* **2022**, *13*, 3165.
- [157] A. I. Komayko, S. V. Ryazantsev, I. A. Trussov, N. A. Arkharova, D. E. Presnov, E. E. Levin, V. A. Nikitina, *ChemSusChem* **2021**, *14*, 1574.
- [158] A. Shrivastava, K. C. Smith, *J. Electrochem. Soc.* **2018**, *165*, A1777.
- [159] J. Peng, J. Wang, H. Yi, W. Hu, Y. Yu, J. Yin, Y. Shen, Y. Liu, J. Luo, Y. Xu, P. Wei, Y. Li, Y. Jin, Y. Ding, L. Miao, J. Jiang, J. Han, Y. Huang, *Adv. Energy Mater.* **2018**, *8*, 1702856.
- [160] S. Baumgart, M. Sotoudeh, A. Groß, *Batteries Supercaps* **2023**, 202300294, <https://doi.org/10.1002/batt.202300294>.
- [161] C. Ling, K. Suto, *Chem. Mater.* **2017**, *29*, 3731.
- [162] E. Levi, E. Lancry, A. Mitelman, D. Aurbach, G. Ceder, D. Morgan, O. Isnard, *Chem. Mater.* **2006**, *18*, 5492.
- [163] T. Kaewmaraya, M. Ramzan, J. Osorio-Guillén, R. Ahuja, *Solid State Ion.* **2014**, *261*, 17.
- [164] E. Levi, G. Gershinsky, D. Aurbach, O. Isnard, *Inorg. Chem.* **2009**, *48*, 8751.
- [165] F. Thöle, L. F. Wan, D. Prendergast, *Phys. Chem. Chem. Phys.* **2015**, *17*, 22548.
- [166] J. Richard, A. Benayad, J.-F. Colin, S. Martinet, *J. Phys. Chem. C* **2017**, *121*, 17096.
- [167] D. Aurbach, Z. Lu, A. Schechter, Y. Gofer, H. Gizbar, R. Turgeman, Y. Cohen, M. Moshkovich, E. Levi, *Nature* **2000**, *407*, 724.
- [168] A. Mitelman, M. D. Levi, E. Lancry, E. Levi, D. Aurbach, *Chem. Commun.* **2007**, 4212.
- [169] H. D. Yoo, I. Shterenberg, Y. Gofer, G. Gershinsky, N. Pour, D. Aurbach, *Energy Environ. Sci.* **2013**, *6*, 2265.
- [170] D. Aurbach, G. Suresh, E. Levi, A. Mitelman, O. Mizrahi, O. Chusid, M. Brunelli, *Adv. Mater.* **2007**, *19*, 4260.
- [171] X. Liu, H. Euchner, M. Zarrabeitia, X. Gao, G. A. Elia, A. Groß, S. Passerini, *ACS Energy Lett.* **2020**, *5*, 2979.
- [172] P. Byeon, Y. Hong, H. B. Bae, J. Shin, J. W. Choi, S.-Y. Chung, *Nature Comm.* **2021**, *12*, 4599.
- [173] R. Chevre, M. Sergent, J. Prigent, *Mater. Res. Bull.* **1974**, *9*, 1487.
- [174] P. Canepa, G. Sai Gautam, D. C. Hannah, R. Malik, M. Liu, K. G. Gallagher, K. A. Persson, G. Ceder, *Chem. Rev.* **2017**, *117*, 4287.
- [175] T. R. Juran, M. Smeu, *Phys. Chem. Chem. Phys.* **2017**, *19*, 20684.
- [176] L. Mei, J. Xu, Z. Wei, H. Liu, Y. Li, J. Ma, S. Dou, *Small* **2017**, *13*, 1701441.
- [177] E. Levi, A. Mitelman, D. Aurbach, O. Isnard, *Inorg. Chem.* **2007**, *46*, 7528.
- [178] E. Levi, A. Mitelman, O. Isnard, M. Brunelli, D. Aurbach, *Inorg. Chem.* **2008**, *47*, 1975.
- [179] M. Smeu, S. Hossain, Z. Wang, V. Timoshevskii, K. Bevan, K. Zaghib, *J. Power Sources* **2016**, *306*, 431.
- [180] J. Rogosic, PhD Thesis, Department of Materials Science and Engineering, Massachusetts Institute of Technology **2014**.
- [181] L. Geng, G. Lv, X. Xing, J. Guo, *Chem. Mater.* **2015**, *27*, 4926.
- [182] B. Lee, H. R. Lee, T. Yim, J. H. Kim, J. G. Lee, K. Y. Chung, B. W. Cho, S. H. Oh, *J. Electrochem. Soc.* **2016**, *163*, A1070.
- [183] Y. Cheng, L. Luo, L. Zhong, J. Chen, B. Li, W. Wang, S. X. Mao, C. Wang, V. L. Sprenkle, G. Li, J. Liu, *ACS Appl. Mater. Interfaces* **2016**, *8*, 13673.
- [184] L. Guohua, H. Ikuta, T. Uchida, M. Wakihara, *J. Power Sources* **1995**, *54*, 519.
- [185] J. Drews, J. Wiedemann, R. R. Maça Alaluf, L. Wang, J. A. Blázquez, Z. Zhao-Karger, M. Fichtner, T. Danner, A. Latz, *Batter. Supercaps* **2023**, *6*, e202200562.
- [186] H. Li, N. L. Okamoto, T. Hatakeyama, Y. Kumagai, F. Oba, T. Ichitsuho, *Adv. Energy Mater.* **2018**, *8*, 1801475.
- [187] C. Delmas, C. Fouassier, P. Hagenmuller, *Physica B+C* **1980**, *99*, 81.
- [188] A. Van der Ven, M. Aydinol, G. Ceder, G. Kresse, J. Hafner, *Phys. Rev. B* **1998**, *58*, 2975.
- [189] J. N. Reimers, J. Dahn, *J. Electrochem. Soc.* **1992**, *139*, 2091.
- [190] C. Delmas, J.-J. Braconnier, C. Fouassier, P. Hagenmuller, *Solid State Ion.* **1981**, *3*, 165.
- [191] A. Van der Ven, G. Ceder, *Electrochem. Solid-State Lett.* **2000**, *3*, 301.
- [192] A. Van der Ven, G. Ceder, M. Asta, P. Tepeesch, *Phys. Rev. B* **2001**, *64*, 184307.
- [193] Y. Mo, S. P. Ong, G. Ceder, *Chem. Mater.* **2014**, *26*, 5208.
- [194] S. P. Ong, V. L. Chevrier, G. Hautier, A. Jain, C. Moore, S. Kim, X. Ma, G. Ceder, *Energy Environ. Sci.* **2011**, *4*, 3680.
- [195] M. S. Whittingham, *Science* **1976**, *192*, 1126.
- [196] M. S. Whittingham, F. R. Gamble Jr, *Mater. Res. Bull.* **1975**, *10*, 363.
- [197] N. A. Godshall, I. Raistrick, R. Huggins, *Mater. Res. Bull.* **1980**, *15*, 561.
- [198] C. Gauckler, M. Dillenz, F. Maroni, L. F. Pfeiffer, J. Biskupek, M. Sotoudeh, Q. Fu, U. Kaiser, S. Dsoke, H. Euchner, P. Axmann, M. Wohlfahrt-Mehrens, A. Groß, M. Marinaro, *ACS Appl. Energy Mater.* **2022**, *5*, 13735.
- [199] S. Daubner, M. Dillenz, L. Pfeiffer, C. Gauckler, M. Rosin, N. Burgard, J. Martin, P. Axmann, M. Sotoudeh, A. Groß, D. Schneider, N. Britta, *Research Square* **2023**. <https://doi.org/10.21203/rs.3.rs-3125461/v1>.
- [200] H. Kim, D.-H. Seo, A. Urban, J. Lee, D.-H. Kwon, S.-H. Bo, T. Shi, J. K. Papp, B. D. McCloskey, G. Ceder, *Chem. Mater.* **2018**, *30*, 6532.
- [201] Z.-L. Tao, L.-N. Xu, X.-L. Gou, J. Chen, H.-T. Yuan, *Chem. Commun.* **2004**, 2080.
- [202] T. R. Juran, M. Smeu, *J. Power Sources* **2019**, *436*, 226813.
- [203] X. Sun, P. Bonnicks, L. F. Nazar, *ACS Energy Lett.* **2016**, *1*, 297.
- [204] A. Emly, A. Van der Ven, *Inorg. Chem.* **2015**, *54*, 4394.
- [205] H.-P. Hong, *Mater. Res. Bull.* **1976**, *11*, 173.
- [206] J. B. Goodenough, H.-P. Hong, J. Kafalas, *Mater. Res. Bull.* **1976**, *11*, 203.
- [207] C. Delmas, F. Cherkaoui, A. Nadiri, P. Hagenmuller, *Mater. Res. Bull.* **1987**, *22*, 631.
- [208] C. Delmas, A. Nadiri, J. Soubeyroux, *Solid State Ion.* **1988**, *28*, 419.
- [209] J. Entwistle, L. Zhang, H. Zhang, N. Tapia-Ruiz, in *Comprehensive Inorganic Chemistry III*, (Eds: J. Reedijk, K. R. Poeppelmeier), 3rd ed., Elsevier, Oxford **2023**, pp. 199–215.
- [210] S. Chen, C. Wu, L. Shen, C. Zhu, Y. Huang, K. Xi, J. Maier, Y. Yu, *Adv. Mater.* **2017**, *29*, 1700431.
- [211] G. F. Ortiz, M. C. López, P. Lavela, C. Vidal-Abarca, J. L. Tirado, *Solid State Ion.* **2014**, *262*, 573.
- [212] C. R. Mariappan, C. Yada, F. Rosciano, B. Roling, *J. Power Sources* **2011**, *196*, 6456.
- [213] M. Hou, F. Liang, K. Chen, Y. Dai, D. Xue, *Nanotechnology* **2020**, *31*, 132003.
- [214] M. Chen, W. Hua, J. Xiao, D. Cortie, W. Chen, E. Wang, Z. Hu, Q. Gu, X. Wang, S. Indris, S.-L. Chou, S.-X. Dou, *Nat. Commun.* **2019**, *10*, 1480.

- [215] Z. Deng, T. P. Mishra, E. Mahayoni, Q. Ma, A. J. K. Tieu, O. Guillon, J.-N. Chotard, V. Seznec, A. K. Cheetham, C. Masquelier, G. Sai Gautam, P. Canepa, *Nat. Commun.* **2022**, *13*, 4470.
- [216] Z. Zhang, Z. Zou, K. Kaup, R. Xiao, S. Shi, M. Avdeev, Y.-S. Hu, D. Wang, B. He, H. Li, X. Huang, L. F. Nazar, L. Chen, *Adv. Energy Mater.* **2019**, *9*, 1902373.
- [217] Z. Zou, N. Ma, A. Wang, Y. Ran, T. Song, Y. Jiao, J. Liu, H. Zhou, W. Shi, B. He, D. Wang, Y. Li, M. Avdeev, S. Shi, *Adv. Energy Mater.* **2020**, *10*, 2001486.
- [218] J. Alamo, *Solid State Ion.* **1993**, *63*, 547.
- [219] T. Asano, A. Sakai, S. Ouchi, M. Sakaida, A. Miyazaki, S. Hasegawa, *Adv. Mater.* **2018**, *30*, 1803075.
- [220] X. Li, J. Liang, N. Chen, J. Luo, K. R. Adair, C. Wang, M. N. Banis, T.-K. Sham, L. Zhang, S. Zhao, S. Lu, H. Huang, R. Li, X. Sun, *Angew. Chem. Int. Ed.* **2019**, *58*, 16427.
- [221] X. Li, J. Liang, J. Luo, M. N. Banis, C. Wang, W. Li, S. Deng, C. Yu, F. Zhao, Y. Hu, T.-K. Sham, L. Zhang, S. Zhao, S. Lu, H. Huang, R. Li, K. R. Adair, X. Sun, *Energy Environ. Sci.* **2019**, *12*, 2665.
- [222] Z. Liu, S. Ma, J. Liu, S. Xiong, Y. Ma, H. Chen, *ACS Energy Lett.* **2021**, *6*, 298.
- [223] B. Helm, R. Schlem, B. Wankmiller, A. Banik, A. Gautam, J. Ruhl, C. Li, M. R. Hansen, W. G. Zeier, *Chem. Mater.* **2021**, *33*, 4773.
- [224] T. Yu, J. Liang, L. Luo, L. Wang, F. Zhao, G. Xu, X. Bai, R. Yang, S. Zhao, J. Wang, J. Yu, X. Sun, *Adv. Energy Mater.* **2021**, *11*, 2101915.
- [225] Q. Shao, C. Yan, M. Gao, W. Du, J. Chen, Y. Yang, J. Gan, Z. Wu, W. Sun, Y. Jiang, Y. Liu, M. Gao, H. Pan, *ACS Appl. Mater. Interfaces* **2022**, *14*, 8095.
- [226] H. Kwak, S. Wang, J. Park, Y. Liu, K. T. Kim, Y. Choi, Y. Mo, Y. S. Jung, *ACS Energy Lett.* **2022**, *7*, 1776.
- [227] M. Feinauer, H. Euchner, M. Fichtner, M. A. Reddy, *ACS Appl. Energy Mater.* **2019**, *2*, 7196.
- [228] J. Hu, K. Chen, C. Li, *ACS Appl. Mater. Interfaces* **2018**, *10*, 34322.
- [229] J. Hu, Z. Yao, K. Chen, C. Li, *Energy Storage Mater.* **2020**, *28*, 37.
- [230] J. Liang, X. Li, S. Wang, K. R. Adair, W. Li, Y. Zhao, C. Wang, Y. Hu, L. Zhang, S. Zhao, S. Lu, H. Huang, R. Li, Y. Mo, X. Sun, *J. Am. Chem. Soc.* **2020**, *142*, 7012.
- [231] L. Zhou, C. Y. Kwok, A. Shyamsunder, Q. Zhang, X. Wu, L. F. Nazar, *Energy Environ. Sci.* **2020**, *13*, 2056.
- [232] S. Muy, J. Voss, R. Schlem, R. Koerver, S. J. Sedlmaier, F. Maglia, P. Lamp, W. G. Zeier, Y. Shao-Horn, *iScience* **2019**, *16*, 270.
- [233] W. Ji, D. Zheng, X. Zhang, T. Ding, D. Qu, *J. Mater. Chem. A* **2021**, *9*, 15012.
- [234] H. Ito, K. Shitara, Y. Wang, K. Fujii, M. Yashima, Y. Goto, C. Moriyoshi, N. C. Rosero-Navarro, A. Miura, K. Tadanaga, *Adv. Sci.* **2021**, *8*, 2101413.
- [235] J. Liang, E. van der Maas, J. Luo, X. Li, N. Chen, K. R. Adair, W. Li, J. Li, Y. Hu, J. Liu, L. Zhang, S. Zhao, S. Lu, J. Wang, H. Huang, W. Zhao, S. Parnell, R. I. Smith, S. Ganapathy, M. Wagemaker, X. Sun, *Adv. Energy Mater.* **2022**, *12*, 2103921.
- [236] R. Schlem, A. Banik, S. Ohno, E. Suard, W. G. Zeier, *Chem. Mater.* **2021**, *33*, 327.
- [237] C. Yu, Y. Li, K. R. Adair, W. Li, K. Goubitz, Y. Zhao, M. J. Willans, M. A. Thijs, C. Wang, F. Zhao, Q. Sun, S. Deng, J. Liang, X. Li, R. Li, T.-K. Sham, H. Huang, S. Lu, S. Zhao, L. Zhang, L. van Eijck, Y. Huang, X. Sun, *Nano Energy* **2020**, *77*, 105097.
- [238] S. Zhang, F. Zhao, S. Wang, J. Liang, J. Wang, C. Wang, H. Zhang, K. Adair, W. Li, M. Li, H. Duan, Y. Zhao, R. Yu, R. Li, H. Huang, L. Zhang, S. Zhao, S. Lu, T.-K. Sham, Y. Mo, X. Sun, *Adv. Energy Mater.* **2021**, *11*, 2100836.
- [239] X. Shi, Z. Zeng, M. Sun, B. Huang, H. Zhang, W. Luo, Y. Huang, Y. Du, C. Yan, *Nano Lett.* **2021**, *21*, 9325.
- [240] N. Adelstein, B. C. Wood, *Chem. Mater.* **2016**, *28*, 7218.
- [241] H. Kwak, D. Han, J. Lyoo, J. Park, S. H. Jung, Y. Han, G. Kwon, H. Kim, S.-T. Hong, K.-W. Nam, Y. S. Jung, *Adv. Energy Mater.* **2021**, *11*, 2003190.
- [242] R. Schlem, T. Bernges, C. Li, M. A. Kraft, N. Minafra, W. G. Zeier, *ACS Appl. Energy Mater.* **2020**, *3*, 3684.
- [243] Y. Qie, S. Wang, S. Fu, H. Xie, Q. Sun, P. Jena, *J. Phys. Chem. Lett.* **2020**, *11*, 3376.
- [244] D. Park, K. Kim, G. H. Chun, B. C. Wood, J. H. Shim, S. Yu, *J. Mater. Chem. A* **2021**, *9*, 23037.
- [245] H. Kwak, J. Lyoo, J. Park, Y. Han, R. Asakura, A. Remhof, C. Battaglia, H. Kim, S.-T. Hong, Y. S. Jung, *Energy Storage Mater.* **2021**, *37*, 47.
- [246] R. Schlem, A. Banik, M. Eckardt, M. Zobel, W. G. Zeier, *ACS Appl. Energy Mater.* **2020**, *3*, 10164.
- [247] E. A. Wu, S. Banerjee, H. Tang, P. M. Richardson, J.-M. Doux, J. Qi, Z. Zhu, A. Grenier, Y. Li, E. Zhao, G. Deysler, E. Sebti, H. Nguyen, R. Stephens, G. Verbist, K. W. Chapman, R. J. Clément, A. Banerjee, Y. S. Meng, S. Ping Ong, *Nat. Commun.* **2021**, *12*, 1256.
- [248] G. Karkera, M. A. Reddy, M. Fichtner, *J. Power Sources* **2021**, *481*, 228877.
- [249] S. K. Sandstrom, X. Chen, X. Ji, *Carbon Energy* **2021**, *3*, 627.
- [250] M. A. Nowroozi, I. Mohammad, P. Molaiyan, K. Wissel, A. R. Munnangi, O. Clemens, *J. Mater. Chem. A* **2021**, *9*, 5980.
- [251] F. Gschwind, G. Rodriguez-Garcia, D. Sandbeck, A. Groß, M. Weil, M. Fichtner, N. Hörmann, *J. Fluor. Chem.* **2016**, *182*, 76.
- [252] B. Sobolev, N. Sorokin, *Crystallogr. Rep.* **2014**, *59*, 807.
- [253] M. Anji Reddy, M. Fichtner, *J. Mater. Chem.* **2011**, *21*, 17059.
- [254] C. Rongeat, M. Anji Reddy, R. Witter, M. Fichtner, *ACS Appl. Mater. Interfaces* **2014**, *6*, 2103.
- [255] C. Rongeat, M. A. Reddy, R. Witter, M. Fichtner, *J. Phys. Chem. C* **2013**, *117*, 4943.
- [256] B. Dieudonné, J. Chable, F. Mauvy, S. Fourcade, E. Durand, E. Lebraud, M. Leblanc, C. Legein, M. Body, V. Maisonneuve, A. Demourgues, *J. Phys. Chem. C* **2015**, *119*, 25170.
- [257] B. Dieudonné, J. Chable, M. Body, C. Legein, E. Durand, F. Mauvy, S. Fourcade, M. Leblanc, V. Maisonneuve, A. Demourgues, *Dalton Trans.* **2017**, *46*, 3761.
- [258] N. I. Sorokin, *Inorg. Mater.* **2004**, *40*, 989.
- [259] L. Liu, L. Yang, M. Liu, X. Li, D. Shao, K. Luo, X. Wang, Z. Luo, *J. Alloys Compd.* **2020**, *819*, 152983.
- [260] I. Mohammad, R. Witter, M. Fichtner, M. Anji Reddy, *ACS Appl. Energy Mater.* **2018**, *1*, 4766.
- [261] B. Cai, Y. Ma, B. Yang, Y. Liu, J. Xia, X. Chen, Z. Li, M.-G. Ju, *Adv. Funct. Mater.* **2023**, *33*, 2300445.
- [262] J. Wang, J. Hao, C. Duan, X. Wang, K. Wang, C. Ma, *Small* **2022**, *18*, 2104508.
- [263] T. Xia, Y. Li, L. Huang, W. Ji, M. Yang, X. Zhao, *ACS Appl. Mater. Interfaces* **2020**, *12*, 18634.
- [264] G. Liu, Y. Wu, Y. Liu, B. Cai, Y. Dong, S. Zhang, H. Zeng, *Appl. Phys. Lett.* **2021**, *119*, 031902.



**Mohsen Sotoudeh** is a postdoctoral researcher and a habilitation candidate at the Institute of Theoretical Chemistry in Ulm University, Germany. He obtained a B.Sc. degree in Physics from Isfahan University of Technology, in 2010, and a M.Sc. degree in Condensed Matter Physics from University of Tehran, in 2013, Iran. He received his Ph.D. degree in Theoretical Physics from the University of Göttingen, Germany, in 2019. His research activities include the areas of first-principles modeling of atomistic structures and processes related to electrochemical energy storage and the search for descriptors to accelerate materials discovery for the new post-lithium energy technologies.



**Sebastian Baumgart** is a Ph.D. candidate in theoretical chemistry at Ulm University, Germany. He received his bachelor's degree in chemistry from RFW University Bonn, Germany in 2017. He then went on to complete his master's degree in chemistry at Ulm University, graduating in 2019. As a member of the EXC2154 "POLiS Cluster of Excellence," his research is focused on discovering novel Prussian blue analogs suitable for application as cathode material in sustainable next-generation batteries.



**Manuel Dillenz** received his B.Sc. and M.Sc. in chemistry from Ulm University including a study semester at Gothenburg University. He is currently a Ph.D. student at the Institute of Theoretical Chemistry at Ulm University under Prof. Axel Groß. His Ph.D. studies involved a research stay at the École Polytechnique Fédérale de Lausanne (EPFL) from August 2022 to October 2022 working with Prof. Nicola Marzari. His research interests include the design of new ionic conductors and structure–composition–property relationships in post-lithium batteries.



**Johannes Döhn** studied physics and energy technology at the Johannes Gutenberg University Mainz and the Technical University of Denmark before he joined the group of Professor Axel Groß at Ulm University as a doctoral researcher in 2020. There, he has been engaged in theoretical research on battery materials but also on electrocatalysis. His battery-related work focuses on the computational evaluation of theoretical battery properties for the material class of perovskites, being especially interested in the development of new materials for so-called post-lithium technologies.



**Katrin Forster-Tonigold** received her diploma in chemistry and her Ph.D. degree in theoretical chemistry from Ulm University, Germany in 2007 and in 2012, respectively. She is currently a postdoctoral researcher at the Helmholtz Institute Ulm, Germany. Her research interest focuses mainly on the modeling of processes at the electrode|electrolyte interface in batteries employing electronic structure methods.



**Katharina Helmbrecht** received her B.Sc. and M.Sc. degrees in chemistry in 2018 and 2020, respectively, from Ulm University, Germany. Currently, she is pursuing her Ph.D. in theoretical chemistry at the same institution, under the mentorship of Axel Groß. Her doctoral research focuses on cathode and solid electrolyte materials for post-lithium batteries. Her expertise lies in magnesium, calcium, and zinc batteries, exploring the potential of the Chevrel phase as a cathode for zinc batteries and the utilization of NASICON materials as solid electrolytes for calcium and magnesium cations.



**Daniel Stottmeister** is a Ph.D. candidate in theoretical chemistry at Ulm University, Germany. He received his bachelor's degree in chemistry from Ulm University, Germany, in 2018. He then completed his master's degree in chemistry at Ulm University, graduating in 2020. As a member of the EXC2154 "POLiS Cluster of Excellence," his research is focused on understanding the formation and the impact of the solid electrolyte interphase in alkali metal batteries.



**Axel Groß** obtained his diploma in physics from the University of Göttingen in 1990 and his Ph.D. in 1993 in theoretical physics at the Technical University of Munich. After 5 years as a staff scientist in the Theory Department of the Fritz-Haber-Institute of the Max-Planck-Society in Berlin, he became Associate Professor in Theoretical Physics/Surface Physics at the Technical University of Munich. In 2004, he was appointed as a Full Professor in Theoretical Chemistry at Ulm University; furthermore, in 2011, he became PI at Helmholtz Institute Ulm (HIU) Electrochemical Energy Storage.